"EL SABER DE MIS HIJOS
HARÁ MI GRANDEZA"

UNIVERSIDAD DE SONORA
DIVISION DE CIENCIAS EXACTAS Y NATURALES
Departamento de Investigación en Física

STRUCTURAL AND ELECTRICAL EXPERIMENTAL STUDIES OF THE CARBON NANOWALL (CNWs) AND RELATED MATERIALS CREATED BY PLASMA-ENHANCED CHEMICAL VAPOR DEPOSITION (PECVD) METHOD AT DIFFERENT DEPOSITION TEMPERATURE

(Thesis presented in option to the scientific degree of Master in Physics)

Author: Lic. Mijaela Acosta Gentoiu

Tutors : Dr. Raul Rierra Aroche, University of Sonora, Mexico
Dr. Gheorghe Dinescu, National Institute of Physics, Magurele, Bucharest
Dr. Lucian Ion, Faculty of Physics, University of Bucharest

Hermosillo, Sonora Febrero, 2015

Universidad de Sonora

Repositorio Institucional UNISON

ACKNOWLEDGMENTS

The present thesis was made in co-operation between the University of Bucharest, Romania, and University of Sonora, Mexico. The work was developed in Romania.

I cannot enough thank to my tutors Dr. Raul Riera, Dr. Gheorghe Dinescu and Dr. Lucian Ion for the development and formation of my thesis.

I want to thanks to the Dr. Raul Riera for the result discussions, preparation and support in the realization of my thesis.

I wish to thank the valuable Dr. Gheorghe Dinescu's direction, National Institute for Laser, Plasma and Radiation Physics (INFLPR), and advisors: Valentina Marascu, Sorin Vitireazu and Daniel Stoica for the development and formation of nano-carbon samples by PECVD device.

Thank to Dr. Lucian Ion, Department of Physics, University of Bucharest, for his great assistance in the interpretation of results and electrical measurements. Also, I appreciate his valuable advice in some moments.

I want to say thanks to Dr. Camelia Florica, Dr. Ionut Enculescu, INFLPR, Dr. Julia Mihalache, National Institute for R&D in Microtechnologies (INTM), and Dr. Daniela Batatorescu, University of Bucharest, for their special support and preparation of electrical measurements. Thanks for his prompt, fruitfull and efficient collaboration. Also, I wish to thank to Ion Burducea, Physics and nuclear engineering institute-Horia Hulubei (IFIN-HH), for his collaboration in hydrogen measurements.

The results of SEM cross-sections on nano-carbon samples made by Camelia Florica and Bogdan Bita, INTM, were very appreciated in this work.

Finally, I want to say thanks to my mother, who always was with me.

Index

INTRODUCTION

Carbon is the sixth most abundant element in nature and forms the basis for all living organisms. In nature there are several carbon kinds of which the best known are graphite, diamond, and amorphous carbon [Wikipedia, graphene]. Carbon like diamond structure disperses light and it has the highest hardness and thermal conductivity of any naturally occurring bulk material. In the form of graphite conducts electricity very well, and it is extremely soft and lubricant [Rochford, 2012].

In the last decades the rapid advance of the science and the nanotechnology made possible to produce nano-carbon with a lot of new special physical and chemical properties, changing shapes, asymmetry, composition, morphology and size [Vizireanu et al., 2012], resulting structures such as carbon nanofibers (CNFs), amorphous carbon nanoparticles (CNPs) and carbon nanowalls (CNWs).

The basic structural element of CNWs and related materials is the ***graphene***. The graphene history began with P. R. Wallace's study in 1947 as a starting point for understanding the electronic properties of 3D graphite. Starting with 1970 "epitaxial graphene" and single layers of graphite were created on top of other materials [Oshima et al., 1987], but the term graphene first appeared in 1987 [Mouras et al., 1987] to describe single sheets of graphite. Efforts to make thin films of graphite started in 1990, [Geim et al., 2008] but nothing was produced in laboratory before 2003. Two Russian-émigré scientists at the University of Manchester, Andrei Geim and Kostya Novoselov, received several awards for their pioneering research on grapheme, notably the 2010 Nobel Prize in Physics [Nobelprize.org, 2010].

In 1985, fullerenes with a zero dimensional structure, were discovered [Sung 2014] and in 1991, Iijima [Iijima, 1991] discovered carbon nanotubes (CNTs) with one-dimensional structures.

Carbon nanofiber synthesis was reported by Boskovic et al., (2002) using a radio frequency PECVD at room temperature. It was subsequently demonstrated by Minea et al. (2004).

Carbon nanowall (CNW) was synthesized by Wu et al. (2002) in an attempt to produce carbon nanotubes (CNT) in PECVD environment. Chuang et al. (2006, 2007) reported the first successful synthesis of CNW by microwave PECVD in various ammonia/acetylene gas mixtures.

Recently, nano-carbon materials have attracted enormous attention owing to their novel mechanical, electronic, and optical properties [Martinu et al., 2010]. The European Union (UE) was the first international community which invested in the nano-carbon research field (1,4 trillion dollars) and created the well-known Graphene Flagship project. Companies like IBM and Nokia already study the tablets creation with resistant carbon materials and translucent screens; besides computers 100 times quicker with chips of graphene circuits are studied. Boeing and Airbus are working in airplanes, whose structures partially made up of graphene could reduce 10% of the airships weight (Blanco, 2013).

The industrial fields have a great interest in these nano-carbon materials, using them in diverse applications such as:

- CNFs material has aplications in catalytic activity [Landis et al., 2010] and polymeric nanocompounds [Haggenmueller et al., 2007]. In recent years CNFs are modified superficially to increase their compatibility toward polymeric material, leading to high interfacial interaction [Fiedler et al,. 2006].
- CNPs can be used into deposited coatings for controlling and improving the tribological properties [Tanenbaum et al., 1996], and reducing the internal stress in the coating film [Hong et al., 2004].
- CNWs material participates in applications such as solar cells, biosensors [Shang et al., 2008], optical and medical devices, thermal management of high density microelectronic components [Hiramatsu et al, 2004], electrodes for energy storage devices [Sung et al, 2014], field emission at low voltages [Wang et al., 2006], membranes for fuel cells and electrodes for battery and supercapacitors [Zhao et al., 2009]. Also, in 2013 were founded manifestations of black body properties. Due to H-termination of the CNWs the film surface is hydrophobic and very stable against structural degradation, especially in a humid environment [Krivchenko et al., 2013]. Also, it has high density of atomic scale graphitic edges that are promising field for electron emission, which might lead to applications in flat panel displays [Hou et al, 2008]. The large surface area is effective as substrate and templates for the fabrication and deposition of other types of nanostructures [Yang et all, 2002].

Despite great theoretical predictions, some of devices fabricated have performed poorly or have been unable to compete with their conventional counterparts (Rochford, 2012). In some cases, the reason for this problem is a lack of understanding or control over the microstructure of the material and their properties. In this paper, we report a study of the structural and electrical properties of the CNWs and related carbon materials, such as CNFs and CNPs, obtained by Plasma-Enhanced Chemical Vapor Deposition (PECVD) method, as well as their synthesis control.

PECVD method allows easily tune structural characteristics of the CNWs and related materials during their synthesis changing certain plasma parameters and substrate conditions. In this paper, we change the deposition temperature from 200^0C to 700^0C keeping constant the other parameters. As result we obtain CNWs and related materials such as CNFs and CNPs.

In that follows, we'll give a brief summary of the six chapters that compound our research work:

In Chapter 1 we briefly introduce different categories of nano-carbon, such as graphene, carbon nanowalls (CNWs), carbon nanofibers (CNFs) and amorphous carbon nanoparticles (CNPs) determined for their structural composition. Also, some electrical properties are described.

The first section of Chapter 2 provides a brief review of the components that integrate PECVD method. Followed by the basic phenomena governing the PECVD processing for the formations and deposition mechanisms of the carbon film. Growth of the CNWs and their growth mechanism on substrate by PCVD method is refer at the end.

In Chapter 3 we made a succinct description of various experimental techniques used in our paper to characterize structural and morphological carbon samples. The methods referred were Fourier Transforms Infrared Spectrometry (FT-IR), X-Ray Diffraction (XRD), Elastic Recoil Detection Analysis (ERDA) and Scanning Electron Microscope (SEM).

In Chapter 4 we refer to the method of electrical measurement of nano-carbon samples. Also, we describe the Semiconductor Characterization System (SCS) device, which is used to measure electrical properties.

In Chapter 5 the resulting carbon films by PCVD at different deposition temperature were characterized in terms of their molecular structure, chemical composition, morphological surface, height and hydrogen composition on surface. The bonding environment and chemical composition of the deposited films were studied by both FT-IR and R-X method. The hydrogen composition on carbon surface was measured by ERDA method and the change of morphology was determined by SEM.

Chapter 6 provides results of electrical measurements from carbon samples deposited on both Cr/Au and platinum electrodes. The changes of electrical properties in carbon samples at room temperature were measured by SCS method. Also, the conduction mechanism was revealed on CNWs through electrical measurements in the temperature range between 3 and 293K.

Chapter 7 rounds up the overall experimental work and measurement results as a conclusion for the thesis.

1. CARBON NANOWALL AND RELATED MATERIALS. GENERALITIES

There are a variety of architectures of carbon film in different morphologies and orientations [Hiramatsu, 2004]. The categories can be determined knowing the sp2 and sp3 hybridization (coordination), level of structural order and the way of arrange of the atoms bond (degree of long range order) and hydrogen concentration (H content), as can see in Figure 1.1

In this context, there are some forms of carbon-based films, such as:

- amorphous hydrogenated carbon (*a*-C:H) or diamond-like carbon (DLC)
- graphite formed by graphene layers
- polycrystalline diamond (pc-D) or nanocrystalline diamond (NCD)
- soft organic carbonaceous coatings (plasma polymers)

The principal carbon phases of hybridization are diamond (sp3) and graphite (sp2). The others carbon structures are intermediate states from this principal phases.

The amorphous and nanocrystalline carbon commonly consist of sp3 and sp2 hybridizations and hydrogen atoms interconnected in a lot of ways that yield different properties.

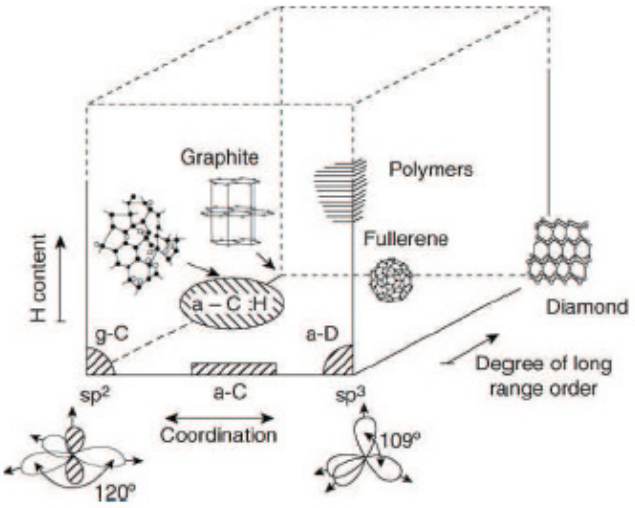

Figure 1.1 Schematic representations of different phases of carbon distinguished by the coordination, degree of range order, and hydrogen content [Casiraghi et al., 2005].

1.1 Graphene

Graphene is a virtually two-dimensional material with nearly transparent layer of pure carbon forming one-atom thick planar sheet. It can also be considered as an indefinitely large aromatic molecule of the family of flat polycyclic aromatic hydrocarbons constituted by a hexagonal arrangement of carbon atoms [Wikipedia, Graphene].
Graphene has high stability due to a tightly packed, periodic array of carbon atoms and sp2 orbital hybridization. Also, it is highly anisotropic [Hummers et al., 1958]. Each

atom has three σ-bonds (with an angle of 120^0 between any two of the bonds) and one π-bond. Graphene presents a combination of orbitals px and py that constitute the σ-bond and pz that constitutes the π-bond. The latter is the key to the half-filled band formation which permits free-moving electrons, conduct electricity and strong bonds between atoms of graphite. As we can see in Figure 1.2, the unit cell, denoted by the dashed box, consists of two atoms, A and B, and is invariant under a 120° rotation about any lattice site. The inter-atomic length is 1.42Å. The lattice can be viewed as two interpenetrating triangular sublattices with lattice vectors a1 and a2 [Rochford, 2012].

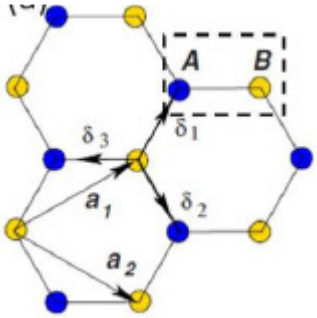

Figure 1.2 Lattice structure of graphene, depicted as two interpenetrating triangle sub-lattices (denoted as yellow and blue circles) with lattice vectors and unit cell marked. δi are the nearest neighbors [Rochford C., 2012].

Graphene has a very low weight: a sheet of 1 square meter only weighs 0,77 milligrams and it is 40 times stronger than steel, translucent and flexible. It is the more resistant and electrical conductor material [Blanco, 2013]. The remarkably high electron mobility with values around of 15,000 $cm^2 \cdot V^{-1} \cdot s^{-1}$[Geim, 2007] under ambient conditions and the transport of charge carriers of 10^{13} per cm^2 made it unique.

Transport is dominated by two modes. One is ballistic and temperature independent, while the other is thermally activated. In ballistic transport, the electrons in graphene are described with the Dirac equation, which has a minimum conductivity on the order of $4e^2/h$. The origin of this minimum is still unclear.

In graphene is characteristic the tunneling effect, which contributes to the extremely high conductivity. In a conventional semiconductor the chance for an electron across the tunnel through a barrier is negligible, while for graphene this transmission occurs, as can see in Figure 1.3.

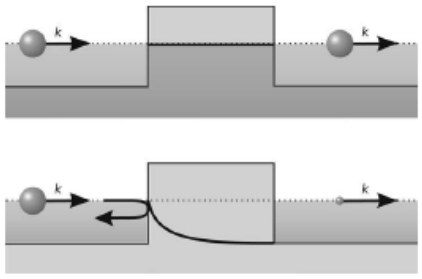

Figure 1.3 Top panel: tunneling in graphene. Lower panel: tunneling in the conventional semiconductor [Katsnelson M., 2006]

1.2 Carbon Nanowalls (CNWs)

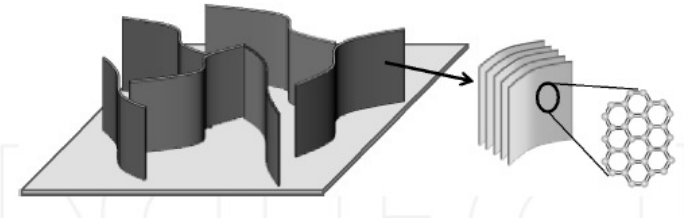

Figure 1.4 Carbon nanowalls [Hiramatsu, 2013]

The carbon nanowalls (CNWs), also called graphene nanowalls (GNWs), graphene nanosheets (GNSSs), and carbon nanoflakes [Chen, 2005], can be described as two dimensional carbon nanomaterials comprising graphene sheets with vertical orientation and random lateral displacement with hundreds of nm spacing on a substrate (see Figure 1.4). The thickness of each sheet has a few tens nanometers, which is the reason for term *nanowall*. CNWs are materials composed of high density of atomic scale graphitic edges. The number of graphene layers is about 1–2 to several 10 sheets [Chengxu et al., 2012] and typically grow between 0,8–2 μm. [Vizireanu et all., 2010]. Compared to a nanotube structure with a thickness of hundreds of microns, the CNWs films are much thinner (only several microns) and it has higher specific light absorption [Krivchenko et al., 2013]. A small bandgap and long coherent length characterize the nanosized bilayer or few layers of graphene sheets [McCann and Lu, 2006].

The wall structures start to grow after an initial layer is formed. Thus, the conductivity of CNWs films is combinations of both CNW and the initial layer. The latter would be horizontal walls formation [Yoshimura et all., 2009] or amorphous carbon (a-C). Therefore, the initial layer is not understood well yet.

The carbon walls are interconnected by a junction point (see Figure 1.5). This property is highly-promising for the functional components of nanoelectronic, biomedical and electron emission nanodevices [Wang et al., 2008] [Shang et all., 2008]. The nanocavities are formed by the inter-connection of two or more CNWs, as show the Figure 1.5. The dimensions of the gaps of these cavities vary from 20 to more 200 nm. These nanocavities may be used as nano-containers for the development of advanced nanofluidic, sensor and separation devices [Yang et al., 2002] [Malesevic et all., 2007]. Nevertheless, CNWs are more complex due to the presence of disorder and defects.

Defects on the CNWs surface performances in applications like catalyst support [Chengxu et al., 2012].

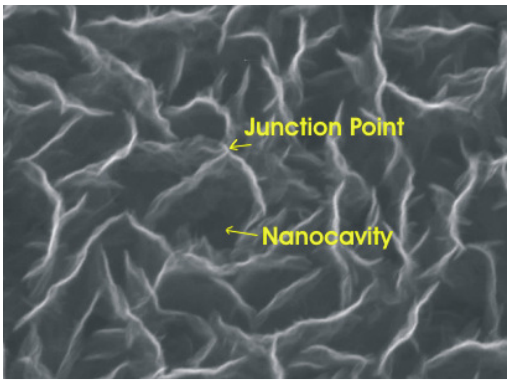

Figure 1.5 SEM image of the CNWs reveals the formation of a nanocavity and shows the junction point for the interconnection of two or more GNSSs.

1.3 Carbon nanofibers (CNFs)

Carbon nanofibers (CNFs) have a cylindrical nanostructure in one dimensional and they could present three phases. The first phase corresponds to the hollow center which is related to the internal diameter of the CNFs. The second one is an ultrathin layer corresponding to amorphous carbon deposited during the synthesis and the third phase belongs to graphene layers [Borjas et al., 2011]. Extremely small graphene sheets are stacked in various directions with respect to the fiber axis [Huang et al., 2010], leading to a surface of CNFs principally made as graphite edges. This characteristic distinguishes the CNFs from CNTs. There are several forms of fiber according to the orientation of the graphitic plane, as can see in Figure 1.6 [Valdés, 2014].

The graphite edge plane sites play roles mainly in the electron-transfer rate and catalytic activity [Landis et al., 2010].

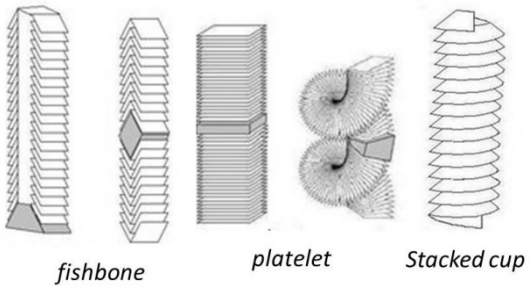

Figure 1.6 Nanofibers types [Valdés, 2014]

1.4 Amorphous hydrogenated carbon (a-C:H)

Amorphous carbon is created when a material containing carbon is burned without enough oxygen. This black soot is known as lampblack [Pierson, 1993].

Hydrogenated amorphous carbon films (a-C:H) have several applications due to their suitable mechanical and chemical properties, such as high hardness (H= 15–40 GPa) and low friction coefficient (μ= 0.05–0.15). The hardening, friction and wear coefficients decrease as the particle size increases [Hong et al., 2004].

There are several amorphous forms due to variations of carbon containing, sp2 and sp3 proportions and hydrogen containing [Clausing et al.,1991] [Pouch et al., 1990]. Therefore, the categories of a-C:H films, as can see in Figure 1.7, are:

- Polymer-like a-C:H (PLCH) with 60% of sp3 hybridizations and the highest hydrogen content (40–50%)
- diamond-like a-C:H (DLCH) with intermediate hydrogen (20–40%) and sp3 contents but presenting good mechanical properties
- hydrogenated tetrahedral amorphous carbon (ta-C:H) with the highest sp3 content (~70%) and around 25% of H atoms
- Graphite-like a-C:H (GLCH) with the lowest hydrogen content (less than 20%), high sp2 proportion, and clustering [Casiraghi et al., 2005].

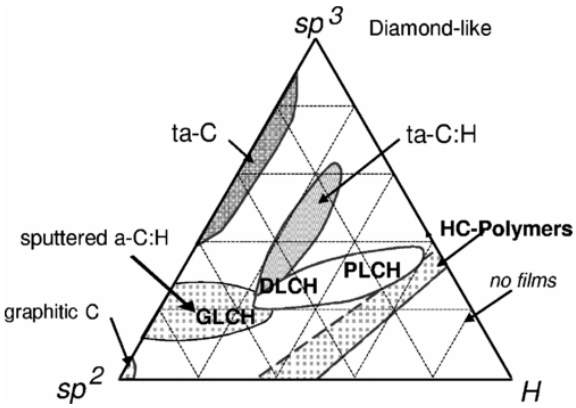

Figure 1.7 Phase diagram of hydrogenated amorphous carbon films (a-C:H) [Casiraghi et al., 2005]

2. PLASMA-ENHANCED CHEMICAL VAPOR DEPOSITION (PECVD) FOR THE OBTAINING CNWS AND RELATED MATERIALS.

Plasma-based technology has the importance to create thin films for a lot of applications. Thus, some techniques have been created:

- physical vapor deposition (PVD) from a solid primary source.
- chemical vapor deposition (CVD) from a gas-phase primary source.
- plasma-enhanced chemical vapor deposition (PECVD) from a gas-phase source with a discharge environment
- vacuum and non-vacuum techniques (sol-gel, flame hydrolysis, electrochemical deposition, thermal-, plasma- and cold-spraying).

In this work we use the radio frequency PECVD technique. It is a process developed to deposit thin films onto a substrate from plasma, which involves reacting gases [Vizireanu, 2008].

PECVD has wide variety of applications becoming one of the most promising techniques for the fabricating of carbon nanomaterial. This technique has allowed synthesize carbon nanoparticles (CNPs), carbon nanowall (CNWs), carbon nanofibers (CNFs) and ultrananocrystalline diamond [Camero et al., 2007] under relatively low pressures using reactive hydrocarbon/argon plasma by different kinds of microwave (MW) [Gruen, 1994] or radiofrequency (RF) discharges [Schulz-von et al., 2001].

For the production of CNWs the PECVD advantages over other fabrication methods are:

- Large scale production with good growth rates
- Feasibility and potentiality
- Relatively low temperatures of deposition (600-700^{0}C).
- Lower chances of cracking deposited layer
- Good step coverage [Cardenas P. and Tung D., 2007]

In this chapter we introduce basic phenomena governing the PECVD process of materials and the mechanism of deposition to obtain carbon film, whose CNWs synthesis is described.

2.1 Generalities

2.1.1 PCVD device components

The PECVD device is presented in the Figure 2.1(a) and its corresponding schematic diagram can be seen in the Figure 2.1 (b). We can see that the PCVD experimental system is formed by 2 chambers named active and reactive (expansion) room.

The active room generates the plasma of radiofrequency. The plasma is enclosed by two parallel electrodes. The upper electrode allows the entrance of gas through cylindrical body, which has typical values 14 mm diameter and 10 mm length. On the other hand, the inferior electrode is a source for the gas expansion towards the reactive room, owing

to the pressure gradient generated between electrodes (2-100 torr). This electrode is a plan disc of diameter 40 mm with an orifice in the center.

The changes of geometry form from the active room, such as the change in distance between electrodes (2-125 mm) and the diameter from the inferior electrode (0.1-4 mm), modify external parameters, such as the plasma pressure.

The reactive room is a cylindrical enclosure with diameter 200 mm and length 1220 mm that allows the control of gases entrance. It has incorporated a screen for seeing the plasma, an oven for heating the system and windows for the pumps.
Plasma, generated into active room, expands through inferior electrode toward the reactive room.

The PCVD is integrated by several components or systems:

- The gas feed and control system
- The pumping system (Roots mechanics pump) and pumping turbo. They work together with Edwards mechanics pump for creating vacuum.
- Oven-controller of temperature
- Computer system
- Pressure system.

These components control some external parameters, such as a power of radiofrequency and flows of gas.

The pumping system
Active room has a vacuum system, which creates vacuum along of gas diffuse. Both mechanical rotational pump (60 m3/h, limit pressure $7,5x10^{-3}$ mbar) and Roots mechanics pump (200 m3/h, limit pressure 8,0x10-4 mbar) creates a minim pressure (around 10^{-3} mbar) into the room. For reach a vacuum improvement is necessary to use the Edwards mechanics pump (with limit value 2.6x10-2 mbar).

Oven-controler of temperature
A suitable oven thermostatic allows heating the substrate at further temperature room, with limit 850^{0} C. The oven system and the supporting with the substrate can be rotated.

Computer system
The previous description shows complex characterization and regulation of parameters. As consequence, a computer system to control the main parameters (the power of radiofrequency, the flows of gas, pressure, temperature etc) is necesary [Vizireanu, 2008].

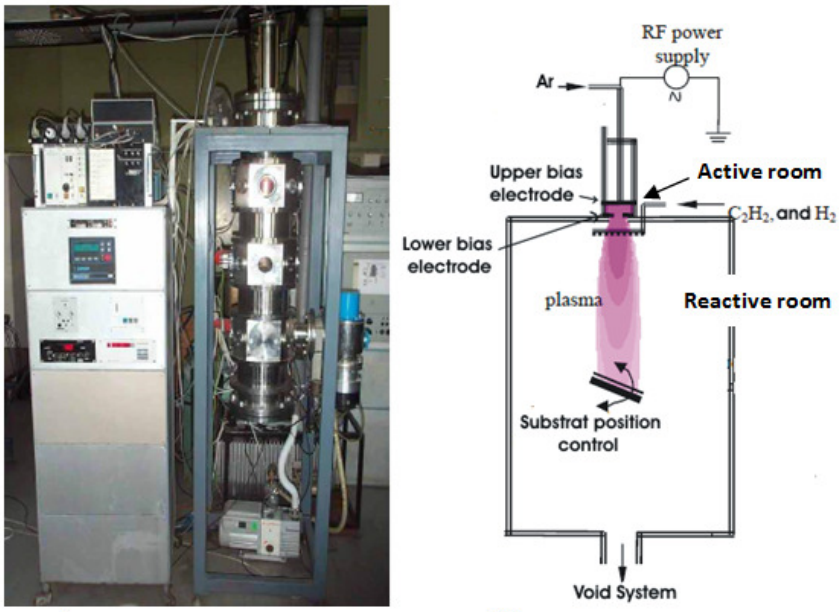

a) b)

Figure 2.1 a) PECVD device used in the present work and b) its schematic diagram [Vizireanu, 2008]

2.1.2 Internal Parameters and Processes into Plasma Bulk of the PECVD method

The performance of external parameters affects internal process into the plasma bulk changing internal parameters, see Figure 2.2. An example is the discharge field frequency over ionization and dissociation of internal process. Higher frequency leads to higher power efficiency and therefore less power is needed to produce one ion–electron pair [Moisan et al., 1991]. Thus, ionization and dissociation process into the plasma bulk are higher in the microwave MW plasma than in radiofrequency RF plasma, generally leading higher densities.

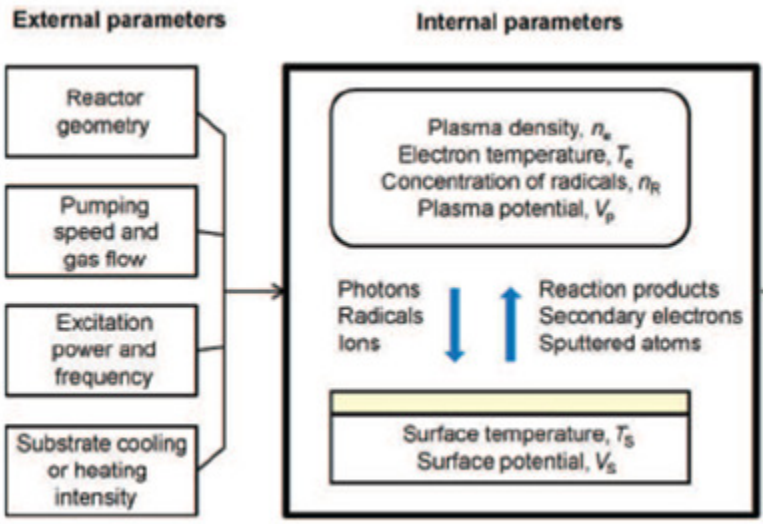

Figure 2.2 Schematic illustrations of internal and external parameters.

Internal parameters are characterized by plasma characteristics, particularly electron density, ρe, electrical potentials, V, and flux of species. We describe these parameters as follow.

2.1.2.1 Plasma potential and surface potential formation

Into the system with electrical discharge, electrons are more mobile than ions. As consequence, a large flux of electrons leaves the plasma and arrives toward substrate before ions. Therefore, the substrate is charged to negative charge and the plasma remains more positive forming potential plasma, Vp. The difference in voltage between the plasma and the substrate normally occurs across a thin sheath region (V_s), as can be seen in Figure 2.3. Ionized atoms or molecules that diffuse to the sheath region feel an electrostatic force and are accelerated towards the surrounding surface. As a consequence, the film exposed to the plasma receives an energetic ion bombardment during deposition. The potential V_s can be approximated by:

$$V_s = (K_B T_e/2e)\ln(m_i/2\pi m_e) \qquad [1]$$

Where T_e is the electron temperature, m_i and m_e are the ion and electron mass respectively.

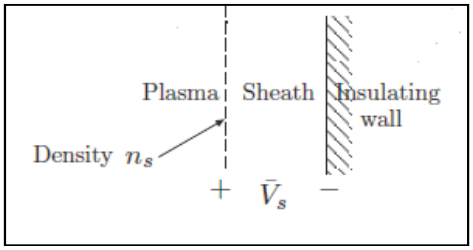

Figure 2.3 The plasma bulk into a potential that across the sheath (Vs) [Lieberman, 2003].

2.1.2.2 Electron and ion temperature

The ion temperature, T_i, in the plasma bulk is less than the electron temperature, T_e, (T_e varies over a narrow range of 2–5V). Instead, when the ion crosses the potential V_s towards the surface, their energy (Ei) surpasses electron energy (Ee). The lower ion energy Ei = e(Vp −Vf), see equation 1, is typically a few times Te, expressed in electron volts, for example for argon plasma the valor resulting is $Ei_{Ar} \approx 4.7k_BTe$ [Lieberman, 2003]. Thus, the ions always acquire some additional energy when diffuse across the sheath [Moisan and Pelletier, 1992]. The energy of the charged particles, which arrive to the surface substrate, can be adjusted by biasing providing DC voltage component, VB, with respect to Vp.

2.1.2.3 Free radical and energetic species formation

Into the bulk plasma, chemically active precursor species (molecular fragments–free radicals, n_R) and energetic species (electrons, ions and photons) are created. These interact in some reactions into the bulk plasma, as can see in table 1. The formed radicals interact further in the gas phase and at the surface, thus ultimately leading to film formation.

Table 1 Basic reactions in active plasma environments.

Reaction	General equation
Reaction with electrons	
Ionization	$e+A \rightarrow A^+ + 2e$
Excitation	$e+A \rightarrow A^* + e$
Dissociation	$e+AB \rightarrow e+A + B$
Dissociative ionization	$e+AB \rightarrow 2e+A^+ + B$
Radiactive recombination	$e+ A^+ \rightarrow A + h\nu$
Reaction between heavy species	
Charge exchange	$A^+ + B \rightarrow A + B^+$
Penning ionization	$A^* + B \rightarrow A + B^+ + e$
Ionization by interchange	$A^+ + BC \rightarrow AB^+ + C$
Combination	$A + B \rightarrow AB$ $AB + CD \rightarrow AC + BD$
Heterogeneus interactions (with surface)	
Metastable deexcitation	$A^* + S \rightarrow A + S$
Sputtering	$A^+ + B_s \rightarrow A + B$

2.2 Synthesis of CNWs and related materials

In this section we present a succinct summary of basic phenomena concerned to reactions involving the argon plasma and acetylene gas, whose interaction with the surface creates CNWs and related materials.

2.2.1 Internal Processes into argon plasma bulk with acetylene gas

Argon plasma is the gas that appears into active camera and it is ionized by radiofrequency electrode. Then, the acetylene (precursor of carbonaceous species) is introduced through a ring into the reactor camera. Various carbon radicals, like CH, CH2, CH3, C2, are formed through excitation and ionization processes into the bulk plasma. Thus, these radicals are transported to the substrate, sustaining the growth of the carbonic material.

2.2.1.1 Excitation and ionization processes of argon gas

The argon specie has an important role in the synthesis, since it is the only species that carries energy from the active room. Also, it carries carbonic radical, which is obtained from dissociation of acetylene, towards substrate to form CNWs.

Ionization and excitation by collision with electrons mainly occurs in the active place through two ways. One way, as a single step occurs by impact with an electron with energy greater than the sum of the ionization energy of the argon atom plus the excitation energy of the formed argon ion:

$$Ar+e \rightarrow (Ar^{+})^{*}+2e \quad [2]$$

In the other way, excitation and ionization occurs by two steps:

$$Ar + e \rightarrow Ar^{+}+2e \quad \text{(Ionization)} \quad [3]$$
$$Ar^{+} + e \rightarrow (Ar^{+})^{*}+2e \quad \text{(Electronic excitation)} \quad [4]$$

The process in two steps has more probability to occur because to the high argon energy (Ei_{Ar}) compared to the electron temperature, Te, in electron volt.

The neutral argon also could impact the ionized atom, thus remain:
$Ar^{+} + Ar \rightarrow 2Ar^{+} + e$

2.2.1.2 Ionization and dissociation processes of acetylene

The argon ion (with Ei_{Ar}= 15.76 eV) and argon metastable (E_i= 11.76eV) have enough energy to dissociate the molecules of acetylene (energy of acetylene is Ei_{C2H2}= 11,41 eV), leading to the fragmentation and radical formation from acetylene with roto-vibrational excited states. Thus, CxHy and $CxHy^{+}$ structures with $1 \leq x \leq 2$ and $1 \leq y \leq 2$ are formed [Janev and Reiter, 2004] [Yasuda, 1985]:

$Ar^{+} + C_2H_2 \rightarrow C_2H_2^{+} + Ar$
$Ar^{*} + C_2H_2 \rightarrow C_2H_2^{+} + Ar + e$
$Ar^{*} + C_2H_2 \rightarrow C_2 + H_2 + Ar$
$Ar^{*} + C_2H_2 \rightarrow CH + CH$

In plasma bulk there exist some electrons with energies greater than the acetylene threshold ionization, being able to create ions in collisions with molecules of acetylene:

$e + C_2H_2 \rightarrow C_2H_2^{+} + 2e$

Moreover, acetylene ions could be impacted by electrons of low energies. Therefore, it appears dissociation reactions, as show table 2. The obtained neutral atom has reduced the threshold ionization owing to the energy released during the dissociative process. Thus, the ionization process can start again from reactions with electronic energies, see table 2.

2.2.1.3 Reaction processes of hydrogen

Interactions of hydrogen molecules with different species into the expansion plasma also occur, the following processes can be observed [Denysenko, 2004]:

$H^+ + C_2H_2 \rightarrow H + C_2H_2^+$
$\rightarrow H_2 + C_2H^+$
$H + CH_2 \rightarrow CH + H_2$
$H_3^+ + C_2H_2 \rightarrow C_2H_3^+ + H_2$
$H_2 + Ar^+ \rightarrow ArH^+ + H$
$\rightarrow Ar + H_2^+$

Excitation, ionization and dissociation processes produced from the hydrogen molecule by electronic interaction can be seen in table 2.

Table 2 Species reaction with electrons

Specie	Reaction with electrons	Result
Ionic acetylene	$C_2H_2^+ + e \rightarrow$	$\rightarrow C_2H + H$
		$\rightarrow C_2 + 2H$
		$\rightarrow CH + CH$
		$\rightarrow C + CH_2$
		$\rightarrow C_2 + H_2$
Neutral atom created from ionic acetylene-electron reaction	$C_2H + e \rightarrow$	$\rightarrow C_2H^+ + 2e$
		$\rightarrow C_2^+ + H + 2e$
		$\rightarrow CH^+ + C + 2e$
		$\rightarrow C^+ + CH + 2e$
		$\rightarrow H^+ + C_2 + 2e$
	$C_2 + e \rightarrow$	$\rightarrow C_2^+ + 2e$
	$CH + e \rightarrow$	$\rightarrow CH^+ + 2e$
	$CH_2 + e \rightarrow$	$\rightarrow CH_2^+ + 2e$
Hydrogen	$H_2 + e \rightarrow$	$\rightarrow H_2^* + e$
		$\rightarrow H_2^+ + 2e$
		$\rightarrow 2H + e$
	$H + e \rightarrow$	$\rightarrow H^* + e$
		$\rightarrow H^+ + e$

2.2.1.4 Interaction with surface

As a result of all these processes stated before, the ions can appear in the plasma with small masses and odd and even number of carbon atoms ($CnHx^+$). These ions are the base of cluster formation in gaseous form through a process of polymerization supported by the remaining acetylene molecules no dissociated from plasma:

$C_nH_x^+ + C_2H_2 \rightarrow C_{n+2}H_x^+ + H_2$ $\quad n\geq 1, x=1\text{-}3$

The discharge into the jet plasma provides a spatial concentration of species that depend of gas and flow rate. Near the point of injection dissociative processes predominate,

leading to the formation of ionic radical and atom with small masses. During the flow the polymerization process starts, concentrations of ions with high masses increase and the original species (precursors) begin to disappear. Thus, at large distances the density of species is reduced even more, including lost by diffusion and deposition on the reactor walls. Also, the hydrogenated molecule decreases monotonically along the flow [Stoica, 2012].

The ion bombardment to the surface can increases the density of the film and removes contaminants, improving the electrical and mechanical properties of the film. Further, when density plasma is sufficiently high, so that the ion density can reach significant sputtering, the bombardment can be employed to flatten the film and fill trenches or holes.

2.2.2 Growth of Carbon nanowalls and their growth mechanism by PCVD method

A mixture of hydrocarbon, in our case C_2H_2, hydrogen and argon gases is used as source gases for the synthesis of CNWs at temperatures range of 500–700˚C. One of the advantages of CNWs is that it can be produced without any catalysts on several substrates, including Si, SiO2, Al2O3, Ni, Ti and other carbon materials. The present section describes the process of CNWs synthesis onto the substrate by PECVD method.

Figure 2.4 depicts the initial growth process on substrate of the CNWs following the next steps:
(1) In the beginning, hydrocarbon radicals are adsorbed on the substrate, forming a very thin amorphous carbon layer on the smooth surface. Ion sputter induces dangling bonds on the surface, resulting in the formation of nucleation sites.

(2) Adsorbed carbon species migrate and condense on the surface to form nanoislands or carbon nanoparticles (CNPs) with dangling bonds. These CNPs are non-uniform in size and shape, and their diameters vary from 10 to 200 nm.

(3) Ion bombardment also enhances the adsorption of CHx radicals on the surface and creates active sites for neutral radical bonding [Zhao et al., 2006]. Film growth under ion bombardment leads effects such as:

- interfacial atom mixing
- high surface mobility (diffusion) of deposited species
- resputtering of loosely bound species

(4) Small, disordered graphene nanosheets predominantly nucleate, grown and connectet with CNPs at their dangling bonds [Chuang et al., 2006]. Then, two-dimensional develop of nanographene with random orientation is formed.

(5) As growth period increases, spreading vertical nanowalls meet one another, eventually resulting in the formation of linked nanowalls similar to a maze [Hiramatsu et al., 2013]. The nanosheets would expand along the direction of radical diffusion, perpendicular to the substrate.
Two models for the growth of the CNWs are reported. The first model supports that CNWs grow up faster in vertically standing nanosheets above amorphous carbon layer,

while the second one refers that the vertically standing walls are developed above nanosheet formations that are horizontal to the substrate surface.

In the first model, the nucleated graphene sheets with random orientations standing almost vertically on amorphous carbon layer. Reactive carbon species arriving onto the nanosheets are easily bonded to the edge.

On the other model, lying graphene sheets are shadowed by the high-grown vertical graphene sheets. Zhu, et al. in 2007 reported the presence of graphenes parallel to the substrate surface as a first layer, before nanosheet vertical growth. The amounts of reactive carbon species arriving upon low-inclined sheet and produce a nanosheets growth above, as consequence the low-inclined sheets are flattened and an initial formation of graphene layer parallel to the substrate is created. Thus, the growth for the inclined smaller nanowalls finish, while the vertical nanowalls preferentially continue growing.

The space between nanowalls increases gradually as increase the growth period [Wu et al., 2004]. The vertical orientation of the sheets may result from the interaction of the plasma electric field with their anisotropic polarizability [Seo et al., 2011].

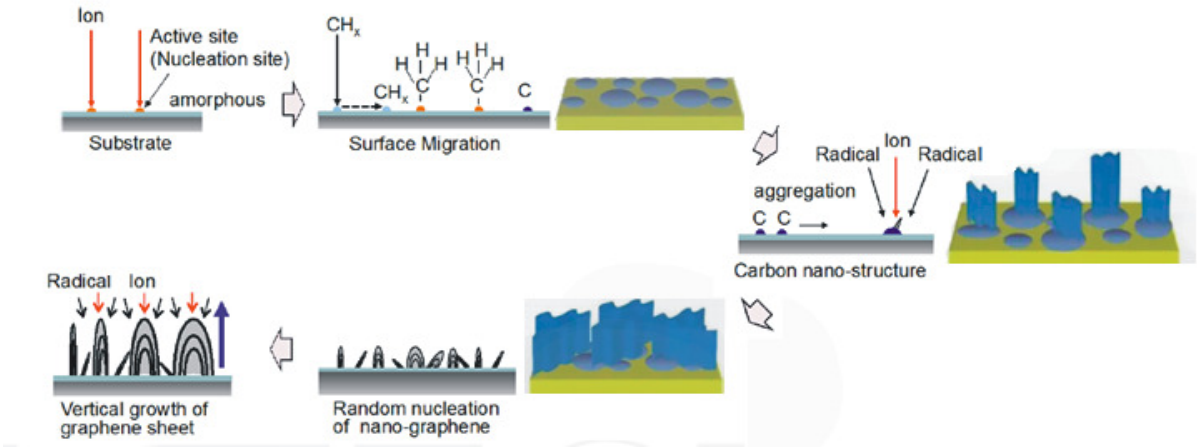

Figure 2.4 Illustration of initial CNW growth.

However, the mechanistic growth scenarios do not clearly explain the critical role of the plasma environment for the nucleation and development of the CNWs patterns and networks with specific architectures and morphologies. It remains essentially unclear how to control the process to achieve either one of the morphologies on the same substrate by a simple adjustment of the plasma process parameters. [Seo et al, 2011].

2.3 Experimental Section to obtain nano-carbon samples

In the synthesis procedure for carbon sample at low pressure, an argon plasma jet is expanding through a nozzle and it is injected with a mixture of acetylene and hydrogen gasses.

In the synthesis of carbon samples, the following parameters were fixed: gas flow ratios Ar/H2/ C2H2: 1 050:25:1 sccm, pressure p=120 Pa, RF power of 300 W and deposition time: 30 min. The substrate was compound of Si material and SiO_2 in the surface. It is collocated at 5 cm distance with the injection ring of acetylene. The conditions mentioned above were selected because they have leading to well defined individual CNWs, with long sharp edges and large areas. The radicals are formed by dissociation of acetylene by collisions in the plasma beam and further transported at substrate.

The temperature was the changed parameter. Gradually, the system was heated up to the pre-determined temperature: 200°C, 300°C, 400°C, 500°C, 600°C and 700°C.

3. METHODS OF STRUCTURAL CHARACTERIZATION OF THE CNWS AND RELATED CARBON MATERIAL

In this paper, the complex carbon structure of the samples is found by a combination of techniques, including Scanning Electron Microscope (SEM), Fourier Transforms Infrared Spectrometry (FT-IR), X-Ray Diffraction (XRD) and Elastic Recoil Detection Analysis (ERDA) Microprobe. These provide detailed information about the microstructure, composition and morphology of carbon films. Throughout this chapter, we briefly refer and describe these different techniques.

3.1 Scanning Electron Microscope (SEM)

3.1.1 Theoretical description

A Scanning Electron Microscope (SEM) reveals information about the sample surface, such as the topography and composition, through scanning with a focused beam of electrons over the sample. The electrons interact with atoms from the specimen to a depth approximately 1 μm, producing various signals that can be collected by detectors with analytical capabilities. Specimens can be observed in high vacuum, in low vacuum and in wet conditions (in environmental SEM) [Wikipedia, SEM].

The mode of signal detection is by secondary electrons (SE) and backscattered electrons (BSE) emitted by atoms excited by the electron beam. Secondary electron is mostly contained on a flat surface and the image has greater resolution. Backscattering electrons appear from electrons incident that losing energy by exciting electrons within the sample material. The escape depth of backscattered electrons can be greater than that the secondary electrons, consequently resolution of topographical characteristics can suffer [Anderson, 2014]. The resulting signal is amplified and displayed on a TV screen or computer monitor with a resolution that can achieve better than 1 nanometer. Different detectors used in SEM can provide several items of data at each pixel, such as the Energy-dispersive X-ray spectroscopy (EDS) detectors and Cathodoluminescence microscope (CL) systems.

Figure 3.1 Illustration for FEI Nova NanoSEM 630, used in the work

3.1.2 Experimental description

In our work, a High Resolution Field Emission Scanning Electron Microscope was used (see Figure 3.1). It was offered by National Institute for R&D in Microtechnologies, Bucharest, Romania. The specifics parameters are: FEI Nova NanoSEM 630, high

resolution FEG-SEM (with Field Emission Gun). The high vacuum has 10^{-4} mBar and the detectors are: ETD, TLD-SE and TLD-BSE.

3.2 Fourier transforms infrared spectrometry (FT-IR)

3.2.1 Theoretical description

Infrared spectroscopy is a no-destructive technique that measures the frequency and intensity of absorption of mid-infrared light by a sample. This method allows investigating the bending and stretching vibrational motions of atoms, as consequence, it is important technique for identification of specified types of chemical bonds, with wide use in organic synthesis [Griffiths and Haseth, 2007].

IR detects frequencies of infrared light from around 4000cm-1 to 400cm-1 that are absorbed by a molecule in the sample. Frequencies with higher wavenumbers have more energy, while frequencies with lower wavenumbers have less energy. Photon energies associated with this frequency (from 1 to 15 kcal/mole) spectrum not excite electrons, since are not large enough. However, the frequencies of infrared light may induce vibrational excitation of bonds that correspond to frequencies of vibrations of covalently bonded atoms. Molecules absorb these frequencies and an IR spectrometer records the light absorbed. Thus, this method allows investigating the bending and stretching vibrational motions of atoms. Also, the physical properties of materials can be correlated to the molecular structure by vibrational spectroscopy better than by any other analytical technique.

Most of the bands that indicate what functional group is present are found in the region from 4000 cm^{-1} to 1300 cm^{-1}. These bands can be identified and used to determine the functional group of an unknown compound. On the other hand, bands that are unique to each molecule are found in the fingerprint region, from 1300 cm^{-1} to 400 cm^{-1}. These bands are only used to compare the spectra of one compound to another.

Fourier transform infrared spectrometry (FT-IR) has improved the measurement of infrared spectra. In FT-IR spectrometry more radiation can be passed between the source and the detector for each resolution. As a result, transmission, reflection, and even emission spectra can be measured quickly [Griffiths and Haseth, 2007].

3.2.2 Experimental description

In this work was employed a Jasco FT/IR-6300A equipment, see figure 3.2, from INFLPR institute, with resolution: 4cm^{-1} and number of accumulations: 1024. The absorption bands are found in the wavenumber region of ν = 4000–500 cm−1.

Figure 3.2 Jasco FT/IR-6300A equipment used in the work.

3.3 X-ray diffraction (XRD)

3.3.1 Theoretical description

X-ray crystallography is a tool used for identifying the atomic and molecular structure of a crystal, as well as their chemical bonds, their disorder and other information.

Crystals are regular arrays of atoms, and X-rays can be considered waves of electromagnetic radiation. Atoms scatter X-ray waves, primarily through the atoms' electrons. Just as an ocean wave striking a lighthouse produces secondary circular waves emanating from the lighthouse, so an X-ray striking an electron produces secondary spherical waves emanating from the electron. This phenomenon is known as elastic scattering, and the electron (or lighthouse) is known as the scatterer. A regular array of scatterers produces a regular array of spherical waves. Although these waves cancel one another out in most directions through destructive interference, they add constructively in a few specific directions, determined by Bragg's law:

$$2d\sin\theta = n\lambda$$

Here d is the spacing between diffracting planes, $\theta$is the incident angle, n is any integer, and λ is the wavelength of the beam. These specific directions appear as spots on the diffraction pattern called reflections [Wikipedia, X-ray crystallography].

Since many materials can form crystals such as salts, metals, minerals, semiconductors, as well as various inorganic, organic and biological molecules, X-ray crystallography has been fundamental in the development of many scientific fields.

3.3.2 Experimental description

The crystalline structure of carbon samples was identified by X-ray diffraction (XRD) with Bragg-Brentano theta-theta geometry, using Cu $K_{\alpha 1}$ (λ= 1.5406A°) as the radiation source. The processing of resulting dates was achieved by Fityk 0.9.8 program.

3.4 Microprobe Elastic Recoil Detection Analysis (ERDA)

3.4.1 Theoretical description

Hydrogen content is also of general interest in characterization of material, since hydrogen can influence the physical and chemical properties. [Petersson et al., 2007] Also, the amount of unbounded hydrogen can be related to density and stress of the sample.

Microprobe Elastic Recoil Detection Analysis (ERDA) is employed for mapping hydrogen isotopes using ion beams as projectiles. When are used slight ions, such as helium, the energy deposited in the sample doesn't affect the original elements. Thus, in our work we measure the hydrogen that underlying trapped in the sample. Although, the helium beam doesn't allows higher cross sections and decline to a greater density of the sample.

The helium ions were produced in cesium sputter ionic sources and are transported to Duoplasmatron chamber. In this chamber they are placed in a channel with sodium plates that changes the charges to produce a negative fascicule. Then, the fascicule is accelerated 3MeV by Magnet Selector into pelletron machine, see Figure 3.3. Afterward, a beam spot is created on the sample and it is focused over the target to remove particles, see Figure 3.4. Finally, a detector receives the hydrogen recoil from the sample.

The relation between the energy of the primary ion before collision (Eprimary) and the energy of the recoiled ion after collision (Erecoil) is given by:

$$K_{recoil} = E_{recoil} \Big/ E_{primary} = \frac{4M_{primary}M_{recoil}}{\left(M_{primary} + M_{recoil}\right)^2} \cos^2 \phi$$

where $M_{primary}$ and M_{recoil} is the mass of the primary ion before collision and after collision respectively, and ϕ is the scattering angle [Tesmer and Nastasi, 1995].

Hydrogen recoiled from deeper in the sample doesn't exhibit the same energy from hydrogen recoils at the surface. The hydrogen energy depends of several parameters such as scattering angle, stopping power in the material and primary beam energy. Furthermore, depending of the sample composition different K_{recoil} will be reached.

3.4.2 Experimental description

The ERDA measurements were performed with the Accelerator Tandetron 3MEV at the "Physics and nuclear engineering institute-Horia Hulubei" (IFIN-HH). It was performed with 3 MeV helium ions and 50 nA current onto spot sample. A 12μm Mylar foil was used as stopper to allow only the entrance of hydrogen into detector. The angle formed between fascicule with the sample and movable detector is 15 and 30grade respectively, see figure 3.5.

A carbon sample with a known amount of hydrogen, H, is used as ETALON sample (pattern). It has 30% of H, 6100 atom/cm^2, height of 510 nm and density 1.4-1.65 g/cm^3. The percent of H in our carbon samples was obtained making a correspondence between the H channel count measurements from our samples and the ETALON pattern. The channel obtained corresponds to energy spectrum.

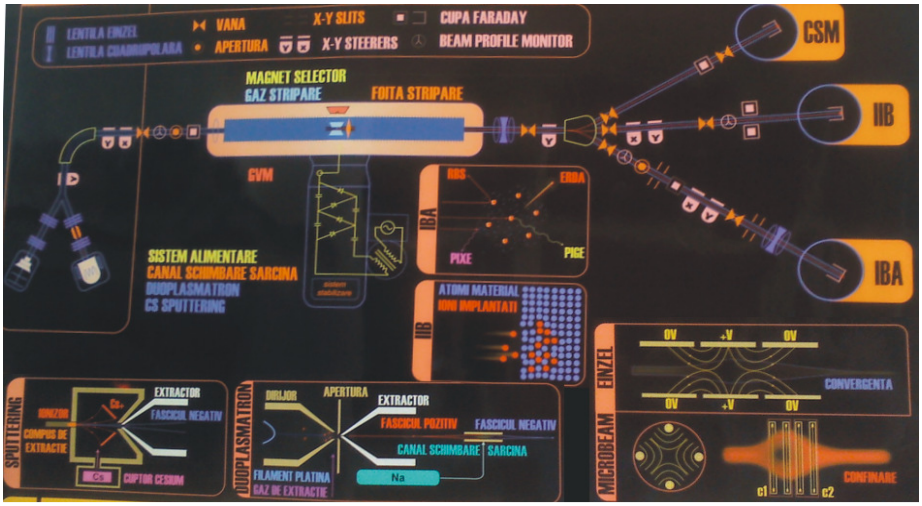

Figure 3.3 System of Accelerator Tandetron 3MEV

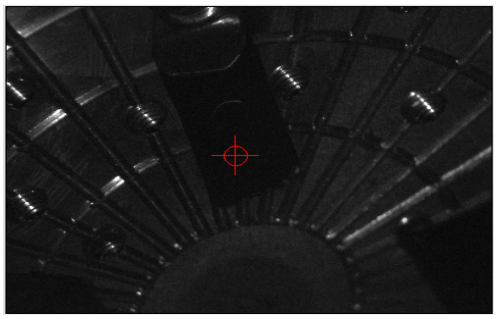
Figure 3.4 The spot beam onto the sample.

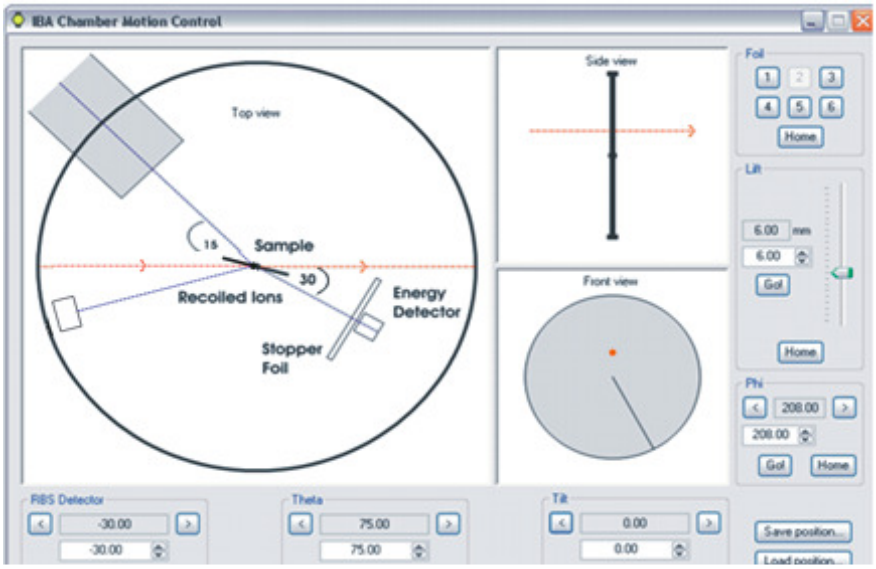

Figure 3.5 Microprobe ERDA, angle formed between fascicule with the sample and movable detector

4. METHODS OF ELECTRICAL CHARACTERIZATION OF THE CNWS AND RELATED CARBON MATERIAL

Throughout this chapter we comment a methodological procedure to the electrical measurement in CNWs and related materials that should be considered in the interpretation of results. Also we refer and describe briefly the Semiconductor Characterization System (SCS) equipment.

For electrical characterization of the CNWs and related materials under study we need to use electrodes for the current–voltage measurement. A constant dc bias was applied across the two terminals from bottom electrodes and the current was measured using the Semiconductor Characterization System (SCS) equipment.

The measurement of the resistance in the horizontal direction to the film was made in the work. Two types of bottom electrodes devices were used: DropSens interdigitated electrodes (IDEs) of Chromium-gold (Ch/Au) material and platinum electrodes with strip configuration. Platinum electrodes are formed by a consecutive distribution of thin strip, achieved by deposition through mask. Both kinds of electrodes are patterned on the substrate of oxide silicon (SiO_2), which is electrically isolate and interact weakly with the nano-carbon sample.

Electrical measurements at room temperature (T_R) were performed in carbon samples at 200^0C, 400^0C, 500^0C and 600^0C deposition temperature using IDEs. In this work, due to an equipment limitation, transport properties in a range of temperature ranging from 3K to 293K were only investigated for the CNWs sample synthesized at 700^0C, using strip electrodes.

4.1 Chromium-gold IDE electrode with carbon samples deposition

DropSens interdigitated electrodes (IDEs) patterns were prepared using the e-beam lithography onto oxide silicon substrate (SiO_2). Figure 4.1(a) shows an example of our electrodes configuration. The IDEs were formed with an inter-finger spacing of 20μm, which are collocated in a consecutive distribution (Figure 4.1(b)).

Figure 4.1 a) Schematic illustrations of IDE electrode probes design before carbon deposition, b) SEM image and c) with carbon deposited by PECVD, where the black circle represents the etched carbon.

Carbon film was grown on the middle position of the IDE (see in Figure 4.1 (c)) by PECVD method at different deposition temperature: 200^0C, 400^0C, 500^0C and 600^0C. A constant dc bias was applied across the two terminals from 0 to 0.5V.

4.2 Platinum trip electrode with CNW deposition

Larger electrode width can be obtained by using a mask of strips as a shield. The pattern to forming the electrode is transferred upon SiO_2 substrate by evaporator system with platinum gas. The strips obtained present a gap of 0,57mm with a consecutive distribution (Figure 4.2 (a) and (b)) and the wide strip is around 0,45mm.

The deposition of carbon upon the electrodes (Figure 4.2 (b)) was performed at both 600^0C and 700^0C deposition temperature by PECVD. A constant dc bias, ranging from 0 to 0,5V, was applied in both samples across the two consecutive strips (see Figure 4.2 (b) represented by below arrows and (c)). Furthermore, in the CNWs sample at 700^0C the electrical measure was performed taking the first strip with the fourth, increasing the gap to 1,71mm (see Figure 4,2 (b), the up arrows). Thus, this electrode configuration would show the electrical behavior at different gaps.

This method of fabrication is simple. The fact that carbon nanowalls are deposited upon any chemical etching is one advantage. This means that the measurements taken are based on untouched carbon structure.

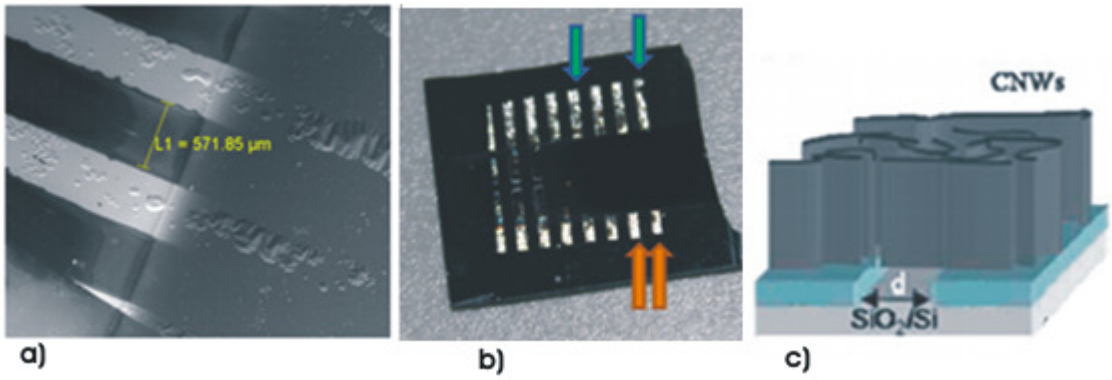

Figure 4.2 a) SEM of platinum electrode device with strip geometry separated by a 0,57mm wide, b) CNW-electrode configuration with the electrical measurement through two consecutive strips, represented by below arrows, and each four strips, represented by up arrows and c) pattern of platinum electrode with CNWs deposition.

4.3 Semiconductor Characterization System with Manual Probe Statio (SCS).

The Semiconductor Characterization System (SCS) equipment, see Figure 4.3, allows electrical measurements for a wide range of applications in materials through I-V characterization. It can measure resistance and conductivity over wide ranges of nanocrystals, nanotubes, nanowires, nanofibres and thin layers. One application is the characterization of nanostructures for electronic nanodevices (diodes, transistors, field efect transistors, capacitors).

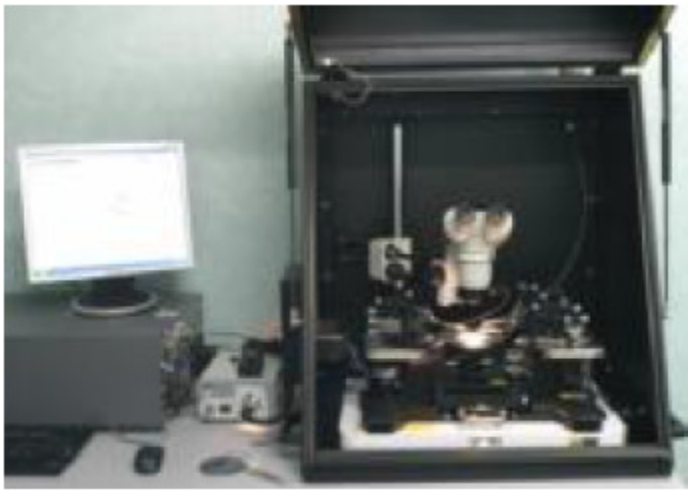

Figure 4,3 Semiconductor Characterization System (SCS) equipment

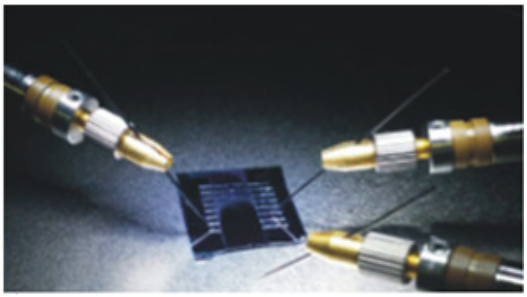

Figure 4,4 Electrical measurement of nano-carbon sample by SCS device.

The SCS used in this work was the Model-4200 SCS/C/Keithley, EP6/ Suss MicroTec Fully programmable for measuring of DC voltage and current simultaneously through two electrodes, as can see in figure 4,4. The characteristic dates are:

- Power: 2.2W (max.105mA, 210V). Per SMU preamplifier: 4200-PA with maximum measurement resolutions: 0.1fA, 5 mV.
- Shielded manual probe station with 4 triaxial cable manipulators.
- Measurements on wafers and substrates up to 150 mm (6“).
- Positioning resolution: 3um.
- Current upgrade status: 2x 4200-SMU and 2x4200-PA.

4.4 Electrical Measurement in a range of temperature ranging from 3K to 293K.

The experimental arrangement includes a closed circuit with Helium cryostat, a temperature controller named Lakeshore, two SourceMeter Keithley 2400 and 6517A Keithley electrometer. The chamber is leaded to vacuum at 10^{-4} Torr for measurement of the CNWs sample at 700^{0}C (deposition temperature), which is mounted on the cryostat finger.

5. MORPHOLOGICAL AND STRUCTURAL CHARACTERIZATION OF THE CNWs AND RELATED MATERIALS AT DIFFERENT DEPOSITION TEMPERATURES

In this section is characterized the composition and microstructure of carbon nanomaterials by FT-IR, XRD and ERDA microprobe method. This is followed by the morphological description through SEM images. Also, a succinct overview of the transition of the nano-carbon materials, governed by the deposition temperature, is depicted.

5.1 Characterization by Fourier Transform Infrared Spectrometry (FT-IR)

The IR spectra tend to be a composite of many different vibrations of C-H bonds, product of mixture of acetylene and hydrogen plasma. The absorption spectrum of carbon material can be observed in Figure 5.1. Here, the absorbance is presented at different temperature and the main peaks spectra were named A, B, C and D. For a better analysis, the spectra is divided in two zones, one between 400-1800cm^{-1} (including the fingerprint region), and the other one between 1800-4000cm^{-1}.

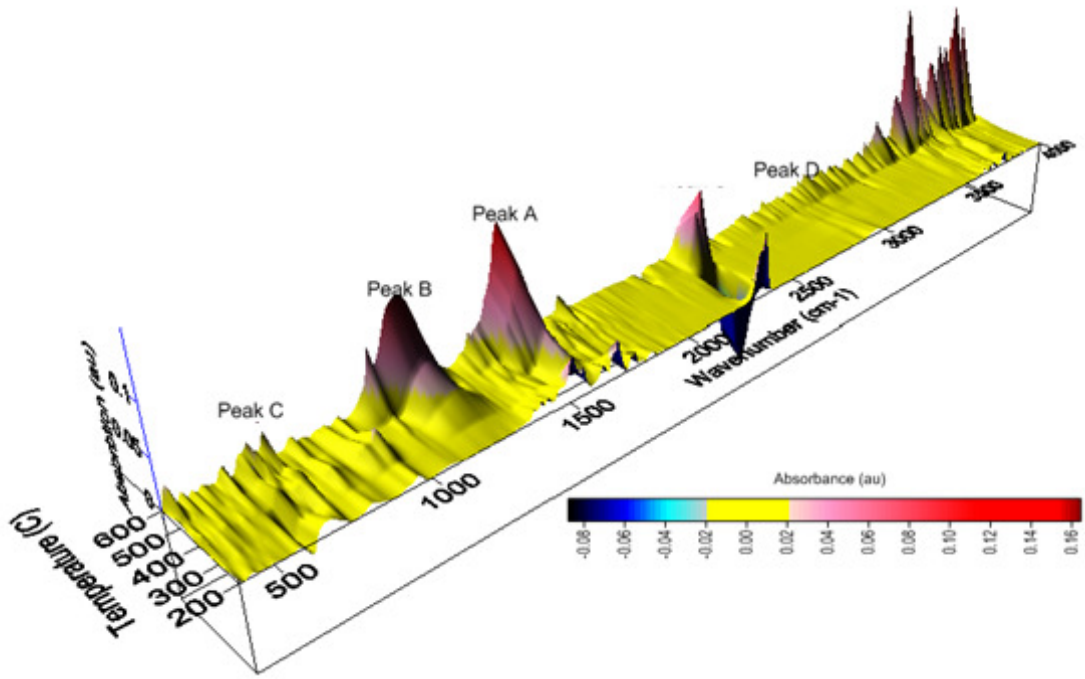

Figure 5.1 3D spectra of carbon material, absorbance vs wavenumber obtained at different temperatures

Region 400-1800

The bands in the region from 400-1800 cm^{-1} originated from interacting vibrational modes resulting in a very complicated series of absorptions, see Figure 5.2. This region contains the fingerprint region, where each organic compound has its own absorption.

We can found an irrelevant peak, around 600 cm^{-1}, produced by the Si substrate and not by the nano-carbon sample, Figure 5.1.

Phenyl rings, characteristic of aromatic structures, appear in all carbon samples related with the sharp peak C (region from 750 to 800 cm^{-1}), see Figure 5.2. The bands between 780 and 960 cm^{-1} are related to the C-C and C-H skeleton vibrations, with the characteristic appearance of structure C-H out-of-plane bending. The peak from 1076 cm^{-1} corresponds to aromatic δ(C-H) in-plane bending vibrations.

The peak B is founded around 1200cm^{-1} for all samples excepting for the carbon structure at 200^{0}C (see Figure 5.1 and 5.2). It represents ν(C-C) stretching vibration [Pretsch et al., 2009]. Also, we can see that the carbon materials signal shifts upward.

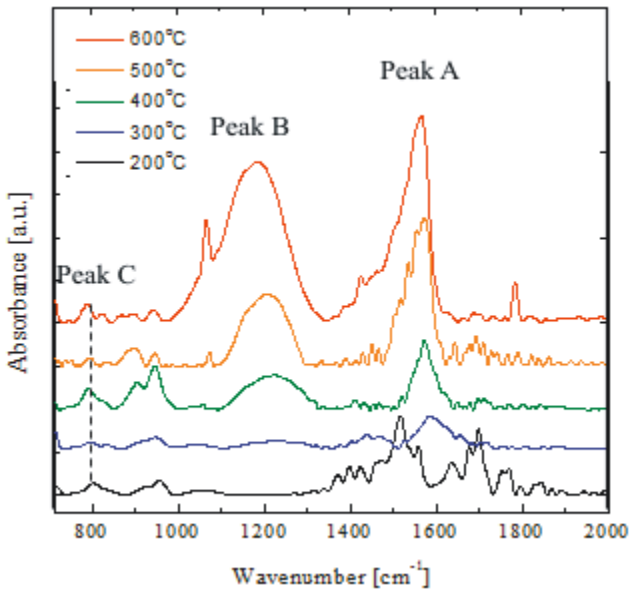

Fig.5.2. FTIR spectra of carbon material obtained at different temperatures in 800-2000cm^{-1} range.

Above 200^{0}C the spectrum is dominated by the peak A (around 1577cm^{-1}) with ν(C=C) stretching vibration, see Figure 5.1 and 5.2. As we can observe, this peak sharply grows with the increasing of the temperature, presenting a linear relation that can be seen in Figure 5.1.

The increase of the temperature allows a prominent emission growth of the C_2 radical at the substrate proximity. It is thought that the concentration of radicals at substrate plays the most important role. As consequence, the crystallinity of the carbon structure improves. The width of the A peak also increases due to the site-to-site variation in the number of next nearest neighbors, that is, when sp2 C atoms have sp3 C neighbors.

The intensity ratio between A and B peak, I(A)/I(B), is kept constant with a value around 2 in the temperature range 300^0C-500^0C deposition, as can see in the Figure 5.3. However, at 600^0C the I(A)/I(B) ratio changes with a decreasing of the value to 1.3, which may be caused by the increase of the disorder in the graphite structure, induced by the coagulation and twisting of graphene sheets.

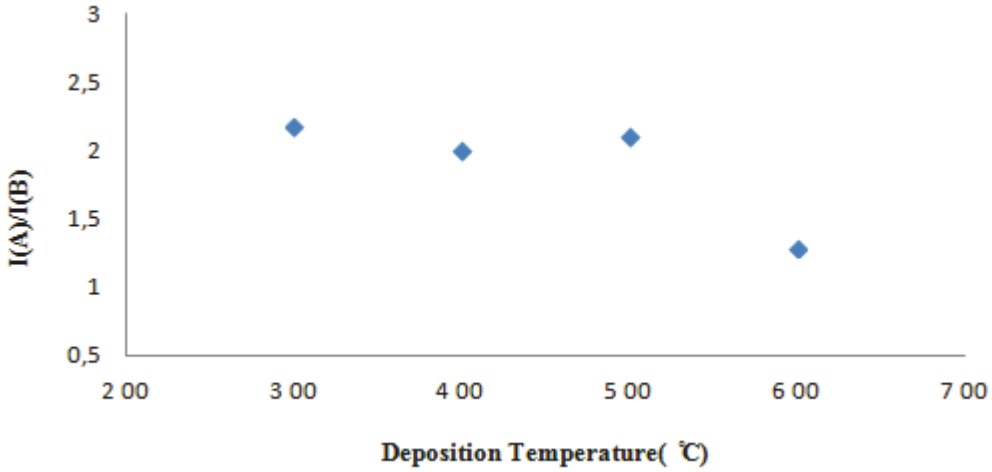

Figure 5.3 The intensity ratios, I(A)/I(B), as a function of the deposition temperature.

Region 1800-4000

The Figure 5.4 presents the region from 2700-3100cm^{-1}, which can also relate the changes in the chemical composition of carbon samples.

The aliphatic stretching $\nu(CH_x)$ bonds, which can be distinguished slightly to the left of the 3000cm^{-1}, are: stretching modes of $\nu(CH_2)$ bonds at 2859 and 2916cm^{-1}, and $\nu(CH_3)$ stretching at 2951 cm^{-1}.

At 3050-3150cm^{-1} region, peak D, is observed the aromatics ν(=C-H) stretching vibration, excluding the sample at temperature 200^{o}C. The increase of this peak with temperature might be explained as the conversion of sp^3 bonds to sp^2 bonds, that means desorption hydrogen and conversion of carbon amorphous to nanocrystalline graphite.

At 200^{o}C temperature we cannot observe the formation aromatics structure. At low temperature, active carbon species lack the mobility to form crystalline carbon [Koh et all., 2010], and there is not a good formation of aromatic compound. Therefore, the difference of carbon spectra at 200^{o}C with other samples is attributed to their difference in structures.

The sample at 600^0C shows disturbances around 3000cm-1 value because complex molecular structures lead to more absorption bands and complex FT-IR spectra, see Figure 5.4, red line.

Environment effects produce tiny peak between 1300-2000cm^{-1} and 3500- 4000cm^{-1} (see Figure 5.1 and 4.2) resulting from the absorption of water vapor (H_2O). Also, can

see near 2350 cm^{-1} (see Figure 5.1) a peak produced by carbon dioxide (CO_2) absorption.

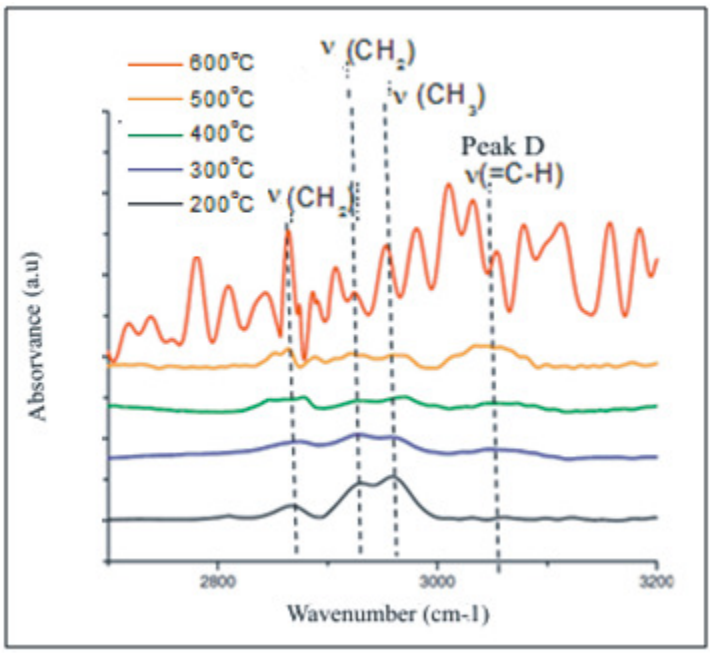

Figure 5.4 FTIR spectra of carbon material obtained at different temperatures in range 2000-3200cm1

5.2 X-Ray Diffraction (XRD)

XRD patterns for CNWs both at 600^0C and 700^0C were shown in Figure 5.5. The diffraction peaks at $27,37^0$, $43,24^0$, $45,40^0$ and $50,00^0$ were observed in the diffraction patterns of CNWs at 600^0C and 700^0C and can be attributed to the graphite structures, (002), (100), (101) and (004) respectively. All the four peaks were similar to the results obtained by Zhang et al. (2012) for CNWs. The peak at $44,36^0$ can be assigned to Si substrate.

The 18°-32° range typically belongs to the graphitic structure. The wide peak is a consequence of combination of two other peaks ($20,69^0$ and $27,37^0$). The maxims, 20,69°, 26,19° and $27,37^0$ have interplanar distances (d): 3,35Å , 3,49Å and 4,36Å respectively. The formation of different interplanar distances may be caused by oxidation processes of CNWs.

The peak intensity grows with the deposition temperature (see Figure 5.5) due to the increase of the C_2 radical at the substrate, according to the FT-IR result.

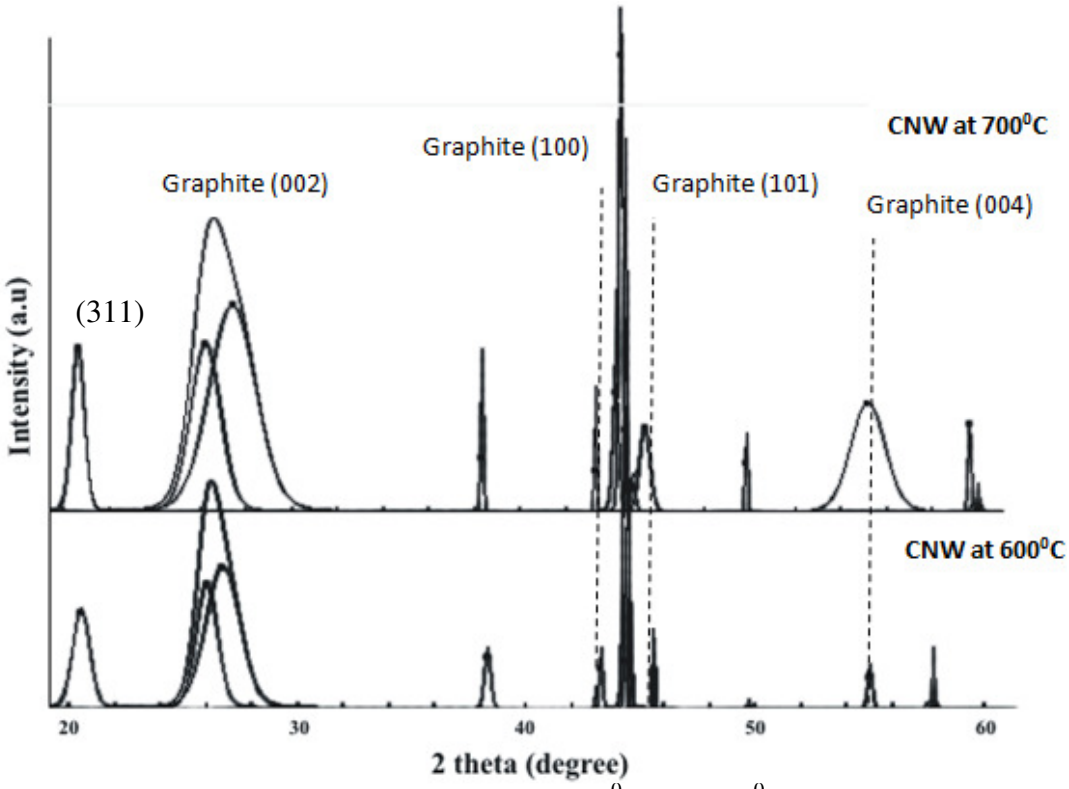

Figure 5.5 X-ray diffraction patterns of CNWs at 600^{0}C and 700^{0}C

5.3 Elastic Recoil Detection Analysis (ERDA)

The spectrum of ETALON sample was measured. It found 2600 channel count, which was related with 30% of Hydrogen. The channel count of nano-carbon samples was related with the ETALON count for obtain the H amount.

Figure 5.6 depicts count spectrum vs channel of carbon samples at different deposition temperature, (a) 200^{0}C, (b)300^{0}C, (c)500^{0}C, and (d) 600^{0}C. The top of the peak was identified with the amount of hydrogen close to the surface. This hydrogen is mainly due to contamination [Bousetta et al., 1994]. Upon 200^{0}C the percent of hydrogen shows a decline with an increasing of deposition temperature (around 9,81%, 7,15% and 2,77% corresponding to 300^{0}C, 500^{0}C and 600^{0}C respectively), this could be associated to the greater degree of graphitization in the structures. The sample at 200^{0}C, with a nanofibers formation, has 5,88% of H on surface. The different arrangement of interconnection between carbon and hydrogen from amorphous and nanocrystalline carbon films are that it leads different form to trap the hydrogen isotopes. The structure of amorphous sample easily traps a significant amount of hydrogen [Raveh, 1992]. On the other hand, the vertically standing of flakes in CNWs and their space between them don't allows a high hydrogen trapping.

In Figure 5.6 a), b), c) and d) the profile for the decline of maxim peak with channel decrement is shown. This represents a reduction of hydrogen amount from depth as helium passes through thickness sample.

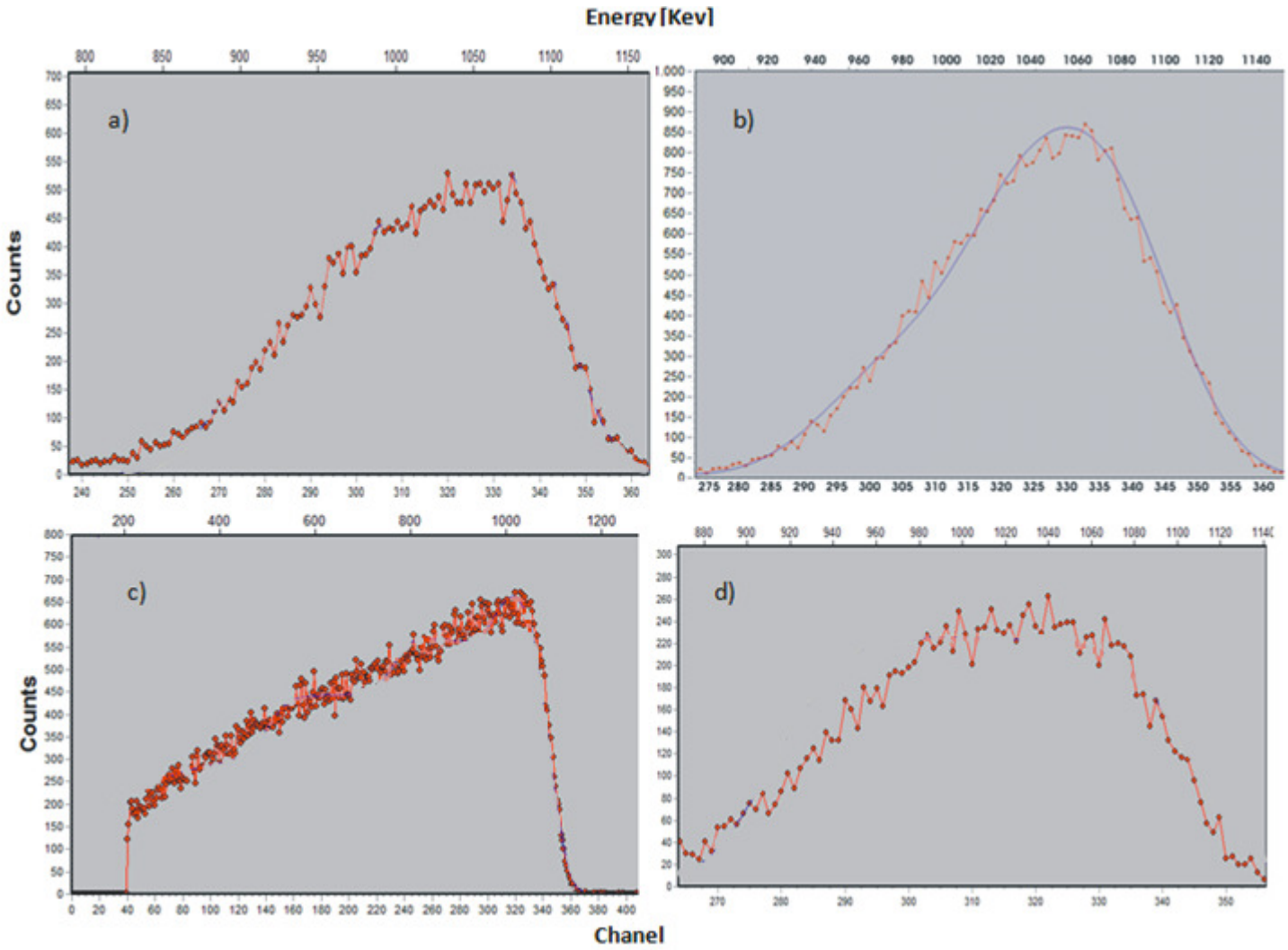

Figure 5.6 ERDA spectrum of nano-carbon samples at different deposition temperature: a) 200^0C, b) 300^0C, c) 500^0C and d) 600^0C.

5.4 Scanning Electron Microscope (SEM)

Scanning electron microscopy (SEM) images of the samples deposited at different deposition temperature are shown in Figure 5.7. The morphology of nano-carbon samples considerably changes, presenting the followed structures: CNFs (at 200^0C), CNPs (at 300^0C and 400^0C), combination between CNPs and CNWs (at 500^0C) and CNWs (at 600^0C and 700^0C).

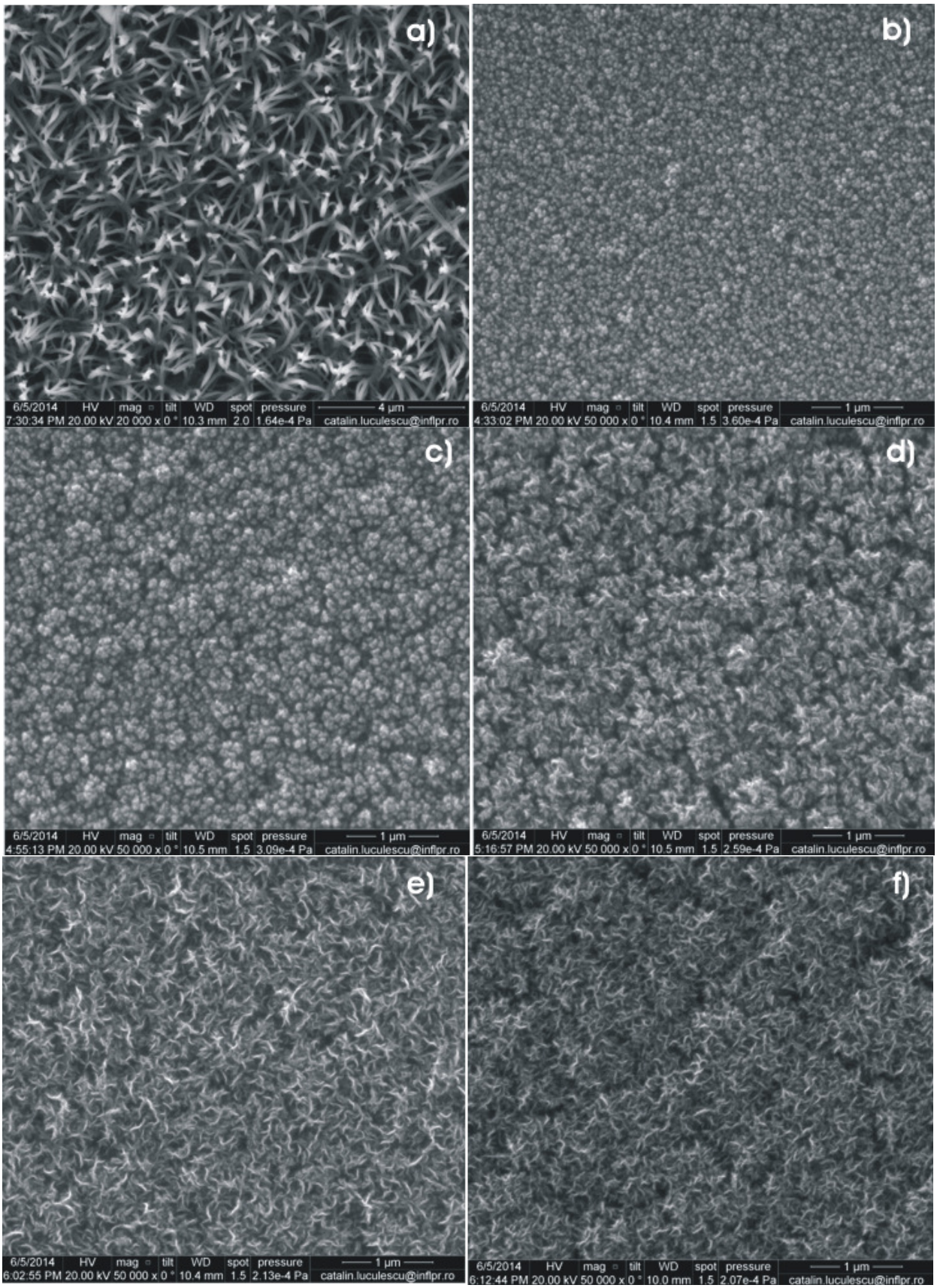

Figure 5.7 Top views by SEM of carbon samples grown on Si substrate using PECVD at different temperatures: a) 200^0C, b) 300^0C c) 400^0C d) 500^0C e) 600^0C and f) 700^0C.

The film height also changes considerably. As can be seen in Figure 5.8 upon 200^0C, the height of the film grows with deposition temperature because appearing more carbon species from the bulk plasma arriving in the surface. The height measurement was obtained by a resolution field SEM.

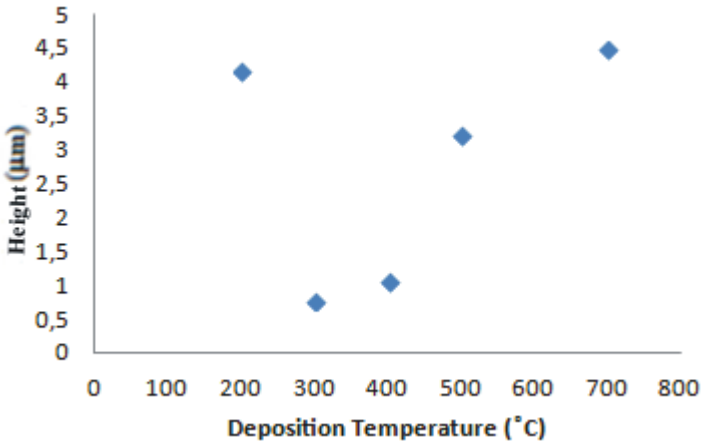

Figure 5.8 Height from carbon samples deposited at different temperature.

5.4.1 Carbon Fibers (CNFs)

Figure 5.7 (a) is the SEM image of the deposition temperature at 200^0C, in which is showed CNFs structure. Here, there is not CNWs formation in agreement with the FT-IR results. As can see, the CNFs are vertically aligned on the Si substrate. They are a height about 4µm and diameter around 47nm, see Figure 5.9.

The low deposition temperature value produces less values of the T_e into the bulk plasma. Therefore, the Te decrement is unfavorable for to excite species with high level of energies, whereas excites other species with less energies level (such as C_2 and CH) [Stoica, 2012]. This effect is only advantageous for CNFs formation.

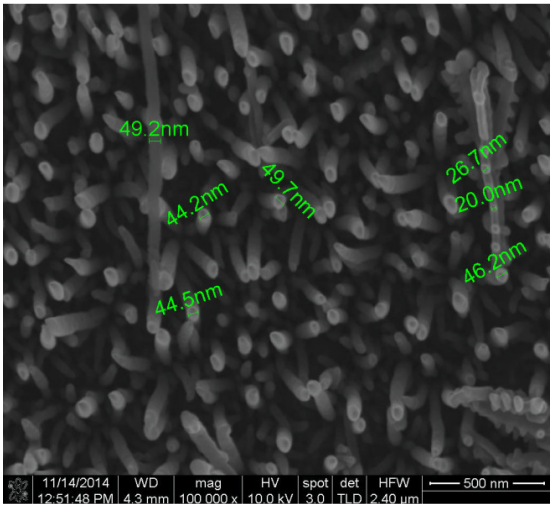

Figure 5.9 SEM of CNFs with the fiber diameter.

5.4.2 Amorphous nanoparticles formation (CNPs)

We show in Figure 5.7 (b) and (c) large nanoclusters with slightly different shapes synthesized at 300^0C and 400^0C respectively. They are produced by nanoparticles agglomerated and embedded in amorphous carbon films, forming carbon nanospheres with amorphous or diamond-like structure (DLC) [Camero et al., 2007].

One can clearly see that the increasing temperature from 300^0C to 400^0C produces the growth of the nanoparticle diameter ranging from 58nm to 147nm, respectively. This corresponds with an increasing in film diameter, as showed in Figure 5.8.

There are formations of nanoparticles within the plasma bulk. Although the growth rate of the particles within the plasma is much faster than on the substrate, the reactive species may lead to the particles deposition on the substrate. With these temperatures values, only CNPs can be produced, which it may be attributed to the shortage of reactive radical formations for the effective nucleation of graphene sheets.

Siegal et al. (2000) and Ohgoe et al. (2005) studied the diamond like carbon films and found sp3 together with sp2 structures, which these are in correspondence with our FT-IR result.

5.4.3 Carbon Nanowalls

CNWs have been detected between 500^0C and 700^0C range, see Figure 5.7 (d), (e) and (f). We can trace the formation of flake-like nanostructures with a longitude around 0,22μm. Also, with an increase of the temperature we can see higher degree of coagulation and agglomeration of nanosheets.

During the nucleation period at 500^0C, graphene component was scarcely contained in the deposition layer as can be seen in Figure 5.7(d) and 5.10. This phase could be intermediate growth stage between CNPs and CNWs, where CNWs start nucleating and growing on the top of CNPs, Figure 5.10.

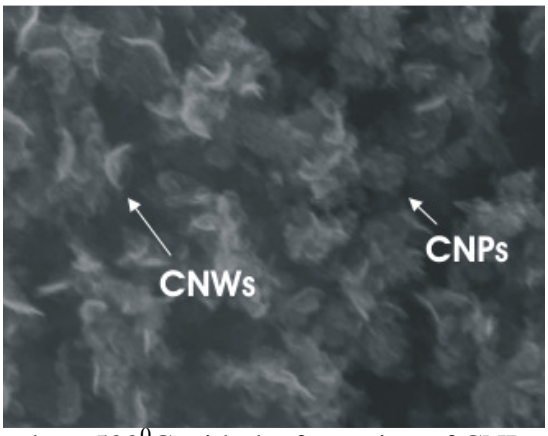

Figure 5.10 Carbon sample at 500^0C with the formation of CNPs and CNWs

At 600^0C the structure contains smaller carbon nanowalls (SCNWs) beside the major carbon nanowall network (CNW), as is clearly seen in Figure 5.11 (a). These smaller carbon nanowalls emerge due to secondary nucleation and they lead to higher surface density of carbon nanowalls. Also, we can see the cross section of CNWs in Figure 5.11(b).

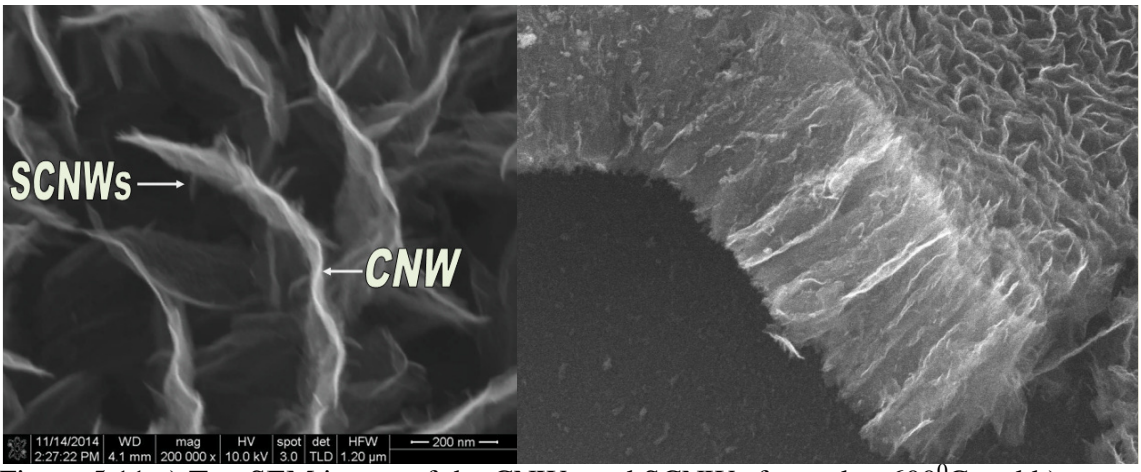

Figure 5.11 a) Top SEM image of the CNWs and SCNWs formed at 600^0C and b) cross section of several layers.

A greater CNWs growth can be seen at higher deposition temperature, 700^0C, corresponding with an increase of height film, Figure 5.7 (f). We conclude, hence, that high temperature produces more dissociation process with the consequent formation of C_2 arriving on the substrate proximity. However, the existing mechanistic growth scenarios do not clearly explain the critical role of the plasma environment in the nucleation and development of the GNSS with specific architectures and morphologies [Seo et al., 2011].

6. ELECTRICAL CHARACTERIZATION OF THE CARBON MATERIAL DEPOSITION BY RF PLASMA BEAM AT DIFFERENT TEMPERATURES

In this chapter we examine the electrical measurement of the carbon sample produced at different deposition temperature onto both IDEs and trip bottom electrode by PECVD. The carbon sample is formed surrounding the electrode, as was explained in chapter 5. At high deposition temperature (700^0C) the SiO_2 substrate not suffered changes, remained similar to those of the surface synthesized by Bange et al. (2008).

The influence of in-plane and in-depth structural anisotroscopy on the current path are not taken into account. Also, the electrical measurement has been reached with low-resistance of electrodes.

6.1 Chromium-gold IDEs electrode with carbon deposition

The electrical resistance presented here corresponds to measurements between the IDEs electrode contacts at room temperature.

In figure 6.1 we can see the electrical resistance measured in carbon samples at different deposition temperature. One can notice upon 300^0C a decreasing in the resistance with the deposition temperature (180,26Ω, 164,38Ω and 160,00Ω corresponding to 400^0C, 500^0C and 600^0C deposition respectively). The minim electrical resistance (77,35Ω) appears at 200^0C deposition with the nanofiber formation.

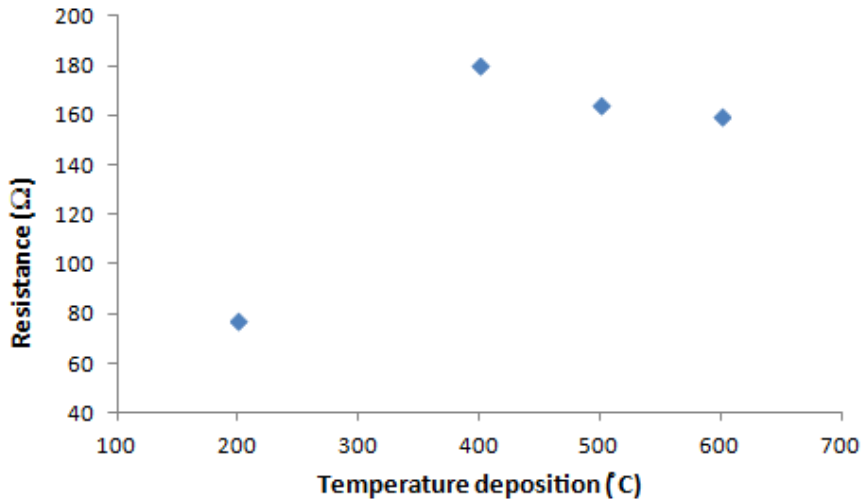

Figure 6.1 The electrical resistance measurement for carbon samples at different deposition temperature, 200^0C, 400^0C, 500^0C and 600^0C, upon chromium-gold IDE electrode.

Carbon sample at 400^0C, corresponding to CNPs structure, has more resistance in comparison to the carbon sample at 600^0C due to higher degree of insulating sp3 bonding and a minor conducting graphitic sp2 bonding. This conclusion is reliable as the results of the FT-IR spectra analyzed in chapter 4, which suggests lower degree of graphitization when deposition temperature decreases.

6.2 Platinum electrode with CNWs deposition

The electrical conductance of the CNWs deposited on silica was measured through two point probe from platinum electrode. Measurements from the sample at 700^0C deposition temperature were carried out in vacuum for the sample temperature (T_M) ranging from 3 K to 293K (approximately room temperature).

6.2.1 Electrical study between 3K and 293K of the CNWs created at 700^0C deposition temperature.

The resistance-temperature graph of CNWs deposited at 700^0C on 0,57mm gap electrode is showed in figure 6.2. It shows a continuous upward trend when the temperature is lowered, with an exponential shape. This reveals a semiconducting nature of the conductivity of the developed CNWs patterns/networks.

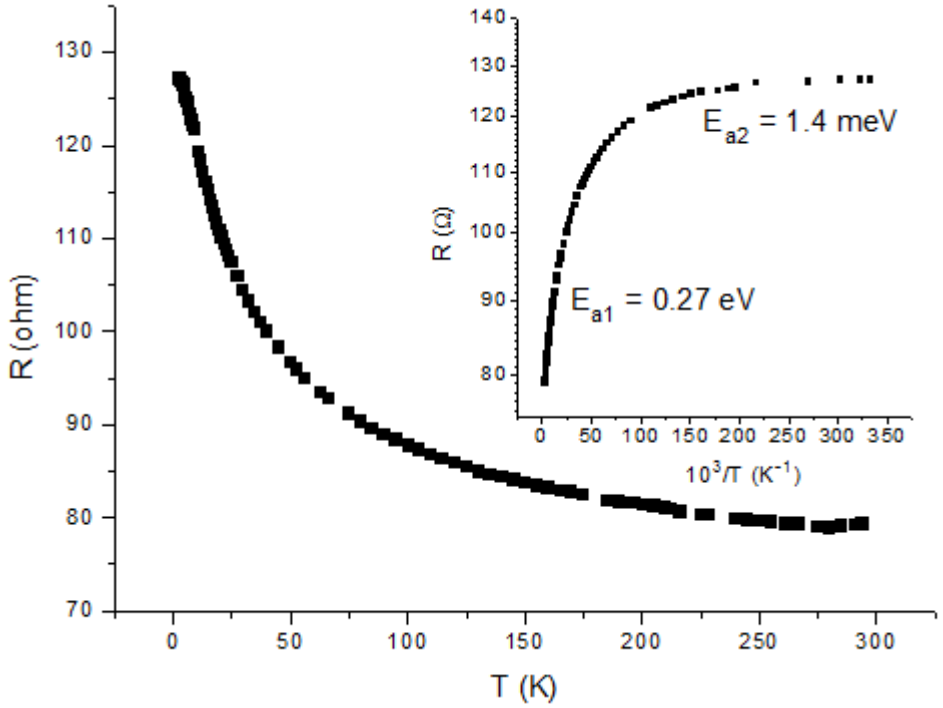

Figure 6.2 Electrical measurement of resistance as a function of Tm of CNWs obtained on silica at 700^0C.

The dependence between temperature (T) and resistance (R) can be fitted using the following equation:

$$R = R_1 e^{\frac{E_{a1}}{k_B T}} + R_2 e^{\frac{E_{a2}}{k_B T}}$$

The first term represents the conduction band contribution, characteristic of the network structure, the latter term could be dominated by hopping resistance of the junctions. The conduction in disordered materials often follows Mott-type variable-range hopping (VRH) model [Mott, 1993]. The first term dominates the 125K – 293K range, while the junction resistance dominates at low temperatures (under ~7K).

The apparent activation energies Ea1 (corresponding to first term) and E_{a2}, (corresponding to second term) for conduction were calculated from the curve fit in figure 6.2 and the obtained values were: 1.4meV and 0.27eV respectively. The thermal activation can be attributed to the influence of thermally-induced carrier excitation across a narrow bandgap.

6.2.2 Electrical study of the 600^{0}C and 700^{0}C deposition temperature CNWs at room temperature

The current-potential graph at room temperature (figure 6.3) of CNWs deposited at 600^{0}C and 700^{0}C on platinum electrode of 0,57mm gap shows a lineal behavior. Also, we can see the electrical resistance.

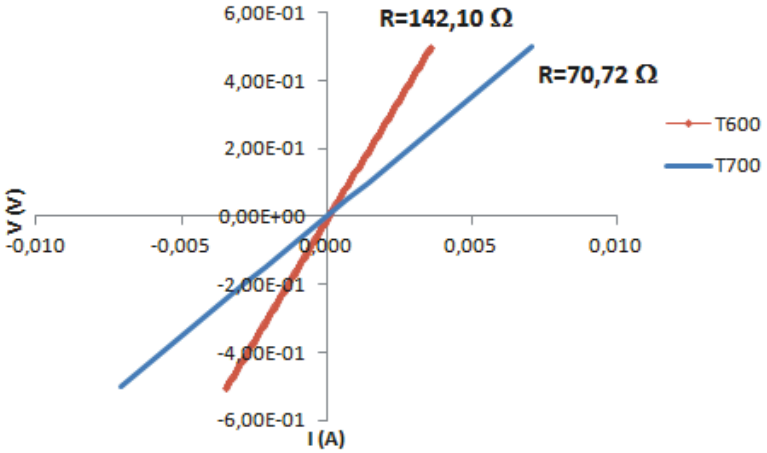

Figure 6.3 The electrical resistance measurement for CNWs at both 600^{0}C (red line) and 700^{0}C (blue line) deposition temperature, on platinum electrode as the 0,57mm gap.

The electrical resistance decreases as increase the deposition temperature (142,10Ω and 70,72Ω corresponding to 600^{0}C and 700^{0}C respectively).

The increase in the sp2 cluster size and crystallinity leads to an increase and formation of the π and π^* bands, thus the band structure becomes more and more continuous, similar to graphite. As consequence, the sample at 700^{0}C has a lower energy barrier for the electron hopping occurs. The higher conduction can be explained by an enhancement of hopping conduction to the highly delocalized π^* band. When the sp2 phase structure becomes more crystalline, the quasimetallic behavior is strengthened due to stronger delocalization of the π^* band.

CNWs structures have defects that create a number of charge traps for the charge carriers, which lead to the resistance. Furthermore, it presents a discontinuous interconnection between nanowall system, featured for the density of voids. These are critical factors that determine the resistance of the CNWs films. Therefore, as the CNWs and graphitization are developed when deposition temperature increase more CNPs will fill the voids and the gap between the vertically oriented nanostructures will

decrease. Thus, the sample at 700^0C has lower resistance compared to the sample at 600^0C deposition.

The sample at 700^0C was measured at room temperature when the gap increases from 0,57mm to 1,71mm at room temperature, thus an increasing of resistance from 70,72 to 176,11Ω respectively was founded. The gaps ratio values (1,71/0,57) and the resistances ratio values (176,11/70,72) are approximate (3 and 2,5 respectively), according with Pouillet low (considering transversal area constant).

7. CONCLUTIONS

In this work we have observed the key role of the deposition temperature in the nanostructure and electrical properties of carbonic films deposited by radio-frequency PECVD. Three formations of nano-carbon structures, CNFs, CNPs and CNWs, have been carried out successfully at 200^0C, 300^0C-400^0C and 500^0C-700^0C ranges, respectively. They were structurally investigated by FT-IR, SEM, R-X and Microprobe ERDA and electrically studied by SCS device. Combining FT-IR, R-X, SEM and Microprobe ERDA results, we conclude that for the 300^0C-700^0C range was produced a structural modification from amorphous carbon film toward polycrystalline graphite, achieving the CNWs formation. By using SCS device, we have obtained the conduction mechanism of the CNWs.

FT-IR result showed a carbon nanostructure formed mostly of carbon atoms in sp2 and sp3 hybridization. The relation sp2/sp3 increased with temperature, corresponding to graphite formation, which became into structure with less hydrogen amount. ERDA Microprobe illustrated that the hydrogen was trapped in the carbonic surface and was decreased with temperature.

At 200^0C, CNFs was formed, according to the SEM image. Unlike the other nano-carbon samples, CNFs had not meaningful aromatics stretch peaks, ν(C-C), ν(=C-H) and ν(C=C), in the IR spectrum. From 750 to 800cm^{-1} (peak C), a phenyl ring is the only aromatic noticeable peak. Consequently, the material has a low order in the crystalline structure.

CNPs with amorphous or diamond-like structure were formed between 300^0C and 400^0C. Through SEM images, we found that the spherical nanoparticle diameter increase from 58nm to 147nm with the upward of temperature. At 500^0C the evolution from small nanospheras to nanosheets was observed, according to the SEM images. Thus, the upward temperature benefits crystalline and nucleation process, which makes possible the CNWs growth. Carbon nanowall film is completely formed above 500^0C and reaches higher graphitic structure at 700^0C, as was observed with R-X.

The increase of the deposition temperature forms active carbon species into the bulk plasma, which produce higher degree of the structural order of nano-carbon material as well as the growth of films height. Here we suggest a critical role of increasing C_2 radicals, which it enables the CNW synthesis.

The electrical conductance from different nano-carbon structure deposited on IDEs electrode was studied using SCS device. Here, we demonstrated that the morphological control of the carbon samples has made possible to achieve difference in the electrical conductance properties. The CNFs formation showed the higher conductance due to his unique structure. Upon 200^0C the conductance in nano-carbon samples enhances with the increasing of the deposition temperature, which is connected with an upward trend in the sp2 content and crystallinity.

The electrical conductance of CNWs at 700^0C deposited on trips electrode was also studied using SCS device. It was electrical measured at different T_M ranging from 3K-293K for his electrical transport study. The resistance-temperature dependence showed a declining exponential behavior as temperature increase. Furthermore, the electrical

measurement revealed that the conduction mechanism in the networks could be described by VRH at less T_M (below ~7K). Comparing electrical measurements at room temperature between the CNWs samples at 600^0C and 700^0C deposition, the latter showed a decrease in the conductance.

Finally, we would like to indicate that there exist a strong dependence between the deposition temperature and the structure of the nano-carbon samples, hence we could obtain a special control over the graphitization of CNWs from the initial nucleation to the final growth stage. This, in turn, will lead to a change in the electrical properties. These results provide a high control and reproducible synthesis of nano-carbon architectures with specific structural and electrical properties for applications in nanoelectronic, sensor, biomedical, optoelectronic components and nanodevices.

BIBLIOGRAPHY

Anderson, Anderson Materials Evaluation, Inc., SEM Illustrative Example: Secondary Electron and Backscatter Electron Images http://www.andersonmaterials.com/sem/, 2014

Bange J. P., L. S. Patil, and D. K. Gautam, Growth and characterization of sio2 films deposited by flame hydrolysis deposition system for photonic device application, 2008, 170.

Boskovic, B.O., Stolojan, V., Khan, R.U., Haq, S., Silva, S.R.P.: Nat. Mater. Large area synthesis of carbon nanofibres at room temperature. Nat. Mater., 2002, 1 ..165.

Blanco D, Grafeno, el material del futuro, Ciencia, Estados Unidos, 2013 http://www.infobae.com/2013/10/21/1517709-grafeno-el-material...

Borjas Ramos J., Téllez Rosas M., F. Ávalos Belmontes, G. Neira Velázquez, F. Ramos de Valle, Caracterización de nanofibras de carbón modificadas superficialmente con plasma de etileno, 2011.

Bousetta A., Lu M., A. Bensaoula, A. Schultz, Appl. Phys. Lett. 65 (6), 1994, 696.

Camero M., Francisco J., Vázquez G., and Gómez-Aleixandre C., Low-Pressure PECVD of Nanoparticles in Carbon Thin Films from Ar/H2/C2H2 Plasmas: Synthesis of Films and Analysis of the Electron Energy Distribution Function, Instituto de Materiales de Madrid (CSIC) 28049 Cantoblanco, Madrid (Spain), 2007

Cardenas P. and Tung D., Plasma Enhanced Chemical Vapor Deposition (PECVD), 2007, http://www.ece.umd.edu/class/enee416.F2007/GroupActivities/Presentation5.pdf,

Casiraghi C., A.C. Ferrari, J. Robertson, Phys., Raman spectroscopy of hydrogenated amorphous carbons, 2005, http://journals.aps.org/prb/abstract/10.1103/PhysRevB.72.085401

Chen C-C, Chen C-F, Lee IH, Lin C-L., Fabrication of high surface area graphitic nanoflakes on carbon nanotubes templates. Diamond Relat Mater, 2005

Chengxu Zhang, Jue Hu, Xiangke Wang, Xiaodong Zhang, Hirotaka Toyoda, Masaaki Nagatsu, Yuedong Meng, High performance of carbon nanowall supported Pt catalyst for methanol electro-oxidation, 2012

Chuang, A. T. H., Robertson, J., Boskovic, B. O., & Koziol, K. K. K. Three-dimensional carbon nanowall structures. *Applied Physics Letters*, 2007, 90(12), 123107

Chuang, A.T.H., Boskovic, B.O., Robertson, J., Freestanding carbon nanowalls by microwave plasma-enhanced chemical vapour deposition. Diam Relat Mater , 2006, 15, 1103

Clausing R., L. Horton, J. Angus, P. Koidl (Eds.), Diamond and Diamond-Like Films and Coatings, Plenum, New York, 1991.

Denysenko I.B., Xu S., Long J.D. and Rutkevych P.P., Azarenkov N.A. and Ostrikov K.J. Appl. Phys. 95 2713, 2004

Fiedler, B., Gojny, F. H., Wichmann, M. H. G., Nolte, M. C. M., Schulte, K. Fundamental Aspects of Nano-Reinforced Composites, Comp Sci. Technol., 66 (16), 3115–3125, 2006.

Geim, A. K., & Novoselov, K. S. The rise of graphene. Nature Materials, 2007, 6, 183-191, nmat1849

Geim, A., Kim, P.,Carbon Wonderland, *Scientific American*, ... bits of graphene are undoubtedly present in every pencil mark" , 2008, (http://www.scientificamerican.com/article.cfm?id=carbon-wonderland).

Griffiths P. R. and Haseth J. A., Fourier transform infrared spectrometry, second edition, University of Idaho Moscow, Idaho, 2007

Gruen D. M., S. Liu, A. R. Krauss, J. Luo, X. Pan X, Appl. Phys. Lett., 1994, 64, 1502.

Haggenmueller, R., Guthy, C., Lukes, J. R., Fischer, J. E., Winey, K. I. Single Wall Carbon Nanotube/Polyethylene Nanocomposites. Thermal and Electrical Conductivity, Macromolecules, 2007, 40 (7), 2417-2421.

Hiramatsu M, Kondo and Hori M, Graphene Nanowalls, Appl. Phys. Lett., 2013, 84, 4708.

Hong S. H., Ph.D Thesis, Ruhr University Bochum 2004.

Hou, K., Outlaw, R. A., Wang, S., Zhu, M., Quinlan, R. A., Manos, D. M., Kordesch, M. E., Arp, U., & Holloway, B. C. (2008). Uniform and enhanced field emission fromchromium oxide coated carbon nanosheets. *Applied Physics Letters*, 92(13).

Huang J, Liu Y, You T. Carbon nanofiber based electrochemical biosensors: a review. Anal Method 2010;2(3):202–11.

Hummers W. S. Jr, R. E. Offeman,"Preparation of graphitic oxide" Journal of the American Chemical Society 1958, 80, 1339.

Iijima, S. Nature 354, 1991, 56–58

Itoh T., Nakanishi Y., Ito T., Vetushka A., Ledinský M., Fejfar A., Kočka J., Nonomura S., Electrical properties of carbon nanowall films, Department of Electrical and Electronic Engineering, Gifu University, Japan, 2012.

Janev R.K., Reiter D., Physics of Plasmas 11, 2, 2004

Katsnelson M., Graphene: carbon in two dimensions, Institute for Molecules and Materials, Radboud University Nijmegen, 6525 ED Nijmegen, The Netherlands, 2006

Krivchenko V. A., S. A. Evlashin,, K. V. Mironovich,, N. I. Verbitskiy,, A. Nefedov,, C. Wöll,, A. Ya. Kozmenkova,, N. V. Suetin,, S. E. Svyakhovskiy,, D. V. Vyalikh,, A. T. Rakhimov,, A. V. Egorov & L. V. Yashina, Carbon nanowalls: the next step for physical manifestation of the black body coating, 2013

Koh ATT, Foong YM, Chua DHC, Cooling rate and energy dependence of pulsed laser fabricated graphene on nickel at reduced temperature, ApplPhys Lett, 2010, 97:114102.

Landis EC, Klein KL, Liao A, Pop E, Hensley DK, Melechko AV, et al. Covalent functionalization and electron-transfer properties of vertically aligned carbon anofibers: the importance of edge-plane sites. Chem Mater, 2010, 22(7):2357–66.

Li X; Zhao, Tianshuo; Wang, Kunlin; Yang, Ying; Wei, Jinquan; Kang, Feiyu; Wu, Dehai; Zhu, Hongwei (**2011**). "Directly Drawing Self-Assembled, Porous, and Monolithic Graphene Fiber from Chemical Vapor Deposition Grown Graphene Film and Its Electrochemical Properties". *Langmuir* 27 (19): 12164–71. doi:10.1021/la202380g (http://dx.doi.org/10.1021%2Fla202380g). PMID 21875131

(https://www.ncbi.nlm.nih.gov/pubmed/21875131).

Li X, Zhao T, Chen Q, Li P, Wang K, (2013), Flexible all solid-state supercapacitors based on chemical vapor deposition derived graphene fibers, http://www.ncbi.nlm.nih.gov/pubmed/24045695

Lieberman M. A., A mini-course on the principles of plasma discharges, 2003, 45

Malesevic A, Vizireanu S, Kemps R, Vanhulsel A, van Haesendonck C, Dinescu G. Combined growth of carbon nanotubes and carbon nanowalls by plasma-enhanced chemical vapor deposition. Carbon 2007, 45:2932–7.

Martinu L., O. Zabeida and J.E. Klemberg Sapieha, Plasma Enhanced Chemical Vapor Deposition of Functional Coatings, Department of Engineering Physics, Canada, 2010.

McCann E., Lu C.L., Phys.: Condens. Matter , Phys. Rev., 2006, 5849

Minea, T.M., Point, S., Granier, A., Touzeau, M.: Appl. Phys. Lett. 85, 1244 Carbon and Oxide Nanostructures: Synthesis, Characterisation and Applications, Appl. Phys. , 2004, Lett.85, 1244

Moisan M., Barbeau C., Claude, R., Ferreira, C.M., Margot, J., Paraszczak, J. Vac. Sci. Technol. B 9, 1991, 8.

Moisan, M. and Pelletier, J., Microwave Excited Plasmas, Elsevier, Amsterdam, 1992.

Mott N., Conduction in Non-Crystalline Materials, 2nd ed. _Oxford Science, New York, 1993.

Mouras, S.; et al., Synthesis of first stage graphite intercalation compounds with fluorides, *Revue de Chimie Minerale,* 1987, 24: 572.
http://cat.inist.fr/?aModele=afficheN&cpsidt=7578318

Ohgoe Y. and Kenji K. Hirakuri, Journal of Applied Physics 2005, 97, 024906.

Oshima, C, Nagashima, A. "Ultra-thin epitaxial films of graphite and hexagonal boron nitride on solid surfaces". *J. Phys.: Condens. Matter* ibcode: JPCM....9....1O, 1997 (http://dx.doi.org/10.1088%2F0953-8984%2F9%2F1%2F004).

Petersson P., Jensen J., Hallén A, Possnert G., Division of Ion Physics, Measurement of hydrogen isotopes by a nuclear microprobe, The Ångström Laboratory, Uppsala University, Sweden, 2007

Pierson, H.O.: Handbook of Carbon, Graphite, Diamond and Fullerenes. William Andrew Publishing, Norwich, 1993.

Pouch J., S.A. Alterovitz (Eds.), Properties and Characterization of Amorphous Carbon Films, Materials, Science Forum, Vols. 52–53, Trans. -Tech., Aedermannsdorf, Switzerland, 1990.

Pretsch E., Philippe B¨uhlmann · Martin Badertscher Structure Determination of OrganicCompounds, pp 279, 2009

Raveh, A., Martinu, L., Gujrathi S.C., Klemberg-Sapieha J.E., Wertheimer M.R., Surf. Coat. Technol. 53, 1992, 275.

Rochford C, Correlating Microstructure and Optoelectronic Performance of Carbon-Based Nanomaterials, Thesis, Kansas University, 2012, 99
http://kuscholarworks.ku.edu/handle/1808/10260

Schulz-von der Gathen V., J. Röpcke, T. Gans, M. Käning, C. Lukas, H. F. Döbele, Plasma Sources Sci. Technol. 2001, 10, 530.

Seo, D. H., Kumar, S., & Ostrikov, K.. Control of morphology and electrical properties of self-organized graphenes in a plasma. *Carbon*, 2011, 49(13), 4331-4339

Shang NG, Papakonstantinou P, McMullan M, Chu M, Stamboulis A, Potenza A, Dhesi SS, Marchetto H, Catalyst-Free Efficient Growth, Orientation and Biosensing Properties of Multilayer Graphene Nanoflake Films with Sharp Edge Planes. Advanced Functional Materials 2008, 18, 3506–3514.

Siegal M. P. and D. R. Tallant, et al. , Physical Review B 2000, 61, 10451.

Stoica s. d., procese fizice asociate sintezei de nanowall-uri de carbon în plasma, thesis, Romania, 2012

Sung Yun Kim, Yeun Ho Joung, and Won Seok Choi (2014), Growth properties of carbon nanowalls on glass substrates by a microwave plasma-enhanced chemical vapor deposition, Japanese Journal of Applied Physics 53, 05FD09, 2014.

Takeuchi W., M. Ura, M. Hiramatsu, Y. Tokuda, H. Kano, M. Hori, Appl. Phys. Lett., 2008, 213, 103.

Tanenbaum D. M., Laracuente A. L., Gallagher A., Appl. Phys. Lett. 1996, 68, 1705.

Tesmer J.R. and Nastasi M., Handbook of Modern Ion Beam Materials Analysis (Pittsburgh: Materials Reasarch Society),1995.

Valdés-Solís T., El descubrimiento de los nanotubos de carbon, 2014, http://www.google.com.cu/url?q=http://naukas.com/2014/01/13/el-descubrimiento-de-los-nanotubos-de-carbono/&sa=U&ei=BpccVP-DG5O8ggSJ2oCwCQ&ved=0CB4QFjAC&usg=AFQjCNH8KrgBrhNEMeQnXGbt3n8Y8Bw6Uw

Vizireanu S., Materiale carbonice obtinute prin tehnici cu plasma, Thesis, Romania, 2008.

Vizireanu S, S D Stoica, C Luculescu, L C Nistor, B Mitu, G Dinescu, Plasma techniques for nanostructured carbon materials synthesis. A case study: carbon nanowalls growth by low pressure expanding RF plasma, Plasma Sources Science and Technology, 19 (2010) 034016 (10pp);

Wang S, Wang S, Miraldo P, Zhu M, Outlaw R, Hou K, Zhao X, Holloway BC, Manos D, Tyler T, Shenderova O, Ray M, Dalton J, McGuire G, High field emission reproducibility and stability of carbon nanosheets and nanosheet-based backgated triode emission devices. Applied Physics Letters. 2006, 89, 183103.

Wang H, Quan X, Yu H, Chen S. Fabrication of a TiO2/carbon nanowall heterojunction and its photocatalytic ability. Carbon 2008, 46:1126–32.

Wikipedia, the free encyclopedia, Graphene

Wikipedia, the free encyclopedia, Scanning electron microscope.

Wikipedia, the free encyclopedia, X-ray crystallography

Wu, Y.H., Qiao, P.W., Chong, T.C., Shen, Z.X.: Adv. Mater. 14, 64 Carbon nanowalls grown by microwave plasma enhanced chemical vapor deposition. Adv. Mater. , 2002, 14, 64

Wu, Y., Yang, B., Zong, B., Sun, H., Shen Z. and Feng, Y., Carbon nanowalls and related materials, J. Mater. Chem., 2004

Yang B, Wu Y, Zong B, Shen Z. Electrochemical synthesis and characterization of magnetic nanoparticles on carbón nanowall templates. Nano Lett 2002, 2:751–4.

Yasuda H., Plasma Polymerization, New York: Academic,1985.

Yoshimura H., S. Yamada, A. Yoshimura, I. Hirosawa, K. Kojima, M. Tachibana,

Chem. Phys. Lett. 482, 2009, 125.

Zhang C., Hu J., Wang X., Zhang X., Toyoda H., Nagatsu M., Meng Y., High performance of carbon nanowall supported Pt catalyst for methanol electro-oxidation, 2012

Zhao X, Tian H, Zhu M, Tian K, Wang JJ, Kang F, Outlaw RA, Carbon nanosheets as the electrode material in supercapacitors. Journal of Power Sources 2009, 194, 1208–1212.

Zhu, M., Wang, J., Holloway, B. C., Outlaw, R. A., Zhao, X., Hou, K., Shutthanandan, V., & Manos, D. M. (2007). A mechanism for carbon nanosheet formation. *Carbon*, 45(11), 2229-2234, j.carbon, 2007